Ore Geology Reviews 101 (2018) 32–53

Contents lists available at ScienceDirect

Ore Geology Reviews

journal homepage: www.elsevier.com/locate/oregeorev

Applications of the combined portable XRF-benchtop SEM methodology to PGE exploration

Yonghua Cao[a,b,*], Robert Linnen[a], David Good[a], Iain Samson[c]

[a] Western University, London, Ontario, Canada
[b] Key Laboratory of Mineralogy and Metallogeny, Guangzhou Institute of Geochemistry, Chinese Academy of Sciences, Guangzhou, Guangdong, China
[c] The University of Windsor, Windsor, Ontario, Canada

ARTICLE INFO

Keywords:
Coldwell complex
PGE
Portable XRF
Benchtop SEM

ABSTRACT

Portable XRF (pXRF) and benchtop scanning electron microscopes equipped with energy dispersive systems (bSEM-EDS) are two real-time analytical techniques that can be combined to collect on-site lithogeochemical and mineral chemical results at dramatically reduced cost and time compared to traditional analytical methods. The Coldwell Complex, northwestern Ontario, is used as a case study on how the combination of these techniques can be applied to mineral exploration. Our results show that whole-rock Ba, V/Ti, Cu/S determined by pXRF, and plagioclase, olivine, and clinopyroxene compositions measured by bSEM-EDS can be applied to exploration for PGE deposits. Cu/S ratios for disseminated sulfides are a proxy for metal tenor, which can be applied as a vector towards higher grade mineralization. Potential magma recharge zones are identified by inspecting down-hole variations in plagioclase, olivine, and clinopyroxene compositions. Fluctuating down-hole variations in these parameters are interpreted to reflect episodic magma recharge. Whether rocks contain PGE mineralization can initially be assessed by documenting the variability of mineral chemistry, i.e., the greater variability of mineral chemistry could be used to vector higher grade PGE mineralization, particularly if the mineralization is conduit-related. Lastly, geochemical mapping of the igneous stratigraphy enables identification of favorable hosts for mineralization. Down-hole whole-rock variations in Ba and V/Ti from pXRF, and mineral chemical profiles from bSEM-EDS are used to discriminate the mineralized Marathon Series from the barren Layered Series throughout the Coldwell Complex. Whole-rock Ba and V/Ti from pXRF and mineral chemical results from bSEM-EDS could prove useful in other settings of the Midcontinent Rift (e.g., the Duluth Complex, Eagle and Eagle East intrusions, Tamarack Intrusive Complex, and the Sonju Lake intrusion) and elsewhere (e.g., the Stillwater Complex) to identify mineralized host rock types. An additional important application is a rapid interpretation of petrogenesis. Down-hole variations in olivine-clinopyroxene Mg-Fe exchange coefficients determined by bSEM-EDS analyses show that olivine-clinopyroxene pairs in the Marathon Series units, particularly for those within PGE mineralized zones, have compositions that are closer to chemical equilibrium (constant) compared to units of the barren Layered Series (highly variable), and thus could be a tool for interpreting petrogenetic processes active in the magma chamber or during the mineralization forming event.

1. Introduction

Recent advances in technologies have resulted in several field portable analytical techniques being developed to collect data in the field at low cost, which facilitates rapid decision making. This includes assays of drill core for ore elements and major and trace element analyses of the hosts rocks to establish a lithogeochemical stratigraphy, which are essential components of mineral exploration. At the Coldwell Complex in northwestern Ontario the laboratory-based results of Good et al. (2015) show that platinum-group element (PGE) in mineralized and barren intrusive rocks are geochemically distinctive, and can be discriminated using Ce vs. Y and Nb vs. Zr diagrams. However, the low concentrations of Ce, Y and Nb in the host gabbros means that these discrimination diagrams are not suited to their application in the field using portable X-Ray fluorescence (pXRF) analyses. Thus, there is a need to develop new discriminant diagrams using elements that can be analyzed by pXRF at the concentrations present in gabbros.

Mineral chemistry is another means of discriminating lithological units and the molar Fe/Mg exchange coefficients between olivine and clinopyroxene ($Kd^{Ol/Cpx}_{Fe/Mg} = (Fe/Mg)_{Ol}/(Fe/Mg)_{Cpx}$) is a fundamental

* Corresponding author at: Western University, London, Ontario, Canada.
E-mail address: ycao84@uwo.ca (Y. Cao).

https://doi.org/10.1016/j.oregeorev.2018.07.006
Received 1 January 2018; Received in revised form 9 July 2018; Accepted 12 July 2018
Available online 20 July 2018
0169-1368/

characteristic of an intrusive unit (Good, 1992; Loucks, 1996). Variations in this coefficient could be useful in correlating units or contacts between drill holes, but analyses of this kind have not been undertaken using field portable instrumentation. However, it is now possible to measure molar Fe/Mg exchange coefficients using a benchtop scanning electron microscopy equipped with energy dispersive spectroscopy (bSEM-EDS). This instrument can easily sit on a table in a field setting and can analyze cut rock and drill core samples without polishing and carbon-coating.

Cao et al. (2016) presented a proof of concept paper that combined pXRF and bSEM-EDS data from a single drill hole and concluded that: 1) pXRF and bSEM-EDS both produce results that are comparable to their lab-based counterparts; 2) the combination of these methods gave a more robust means of distinguishing between different gabbro series than by pXRF only; 3) whole rock Cu/S ratios can be used as a proxy for Pd grades; and 4) platinum group minerals can be identified in drill core samples by bSEM-EDS with minimal sample preparation.

The current work builds on the proof of concept study and tests the application of the combined pXRF-bSEM-EDS approach to PGE exploration by examining drill holes from three areas of the Eastern Gabbro of the Coldwell Complex. New data was collected to 1) develop new discriminants that can be analyzed by pXRF and evaluate whether these discriminants are applicable to other deposits in the Midcontinent Rift and elsewhere; 2) test whether the combined pXRF-bSEM-EDS can be applied to igneous stratigraphic mapping at the scale of an intrusion; 3) apply $Kd^{Ol/Cpx}_{Fe/Mg}$ values from bSEM-EDS to evaluate processes such as undercooling, and 4) evaluate whether the integration of pXRF-bSEM-EDS can be used to identify possible magma conduits.

2. Geological setting

The Coldwell Complex is the largest alkaline complex in North America and is related to the Midcontinent Rift (Fig. 1). It is a subcircular composite pluton that has a diameter of approximately 25 km and a surface area of 580 km^2 (Walker et al., 1993). It intruded the Archean Schreiber-White River greenstone belt during the early stages of Midcontinent Rift development (Walker et al., 1993; Heaman et al., 2007). The Eastern Gabbro suite constitutes the oldest part of the Coldwell Complex. It occurs along the eastern and northern margin of the complex (Fig. 2) and comprises numerous cross-cutting gabbroic and ultramafic intrusions that were emplaced into a thin meta-volcanic package (Good et al., 2015).

Shaw (1994, 1997) interpreted that the Eastern Gabbro formed by multiple intrusions of basaltic magma into a partial ring-dike structure that cut the Archean country rock. The Eastern Gabbro Suite consists of a diverse assemblage of discrete gabbroic intrusions that cut a less than 1 km-thick package of the Metabasalt (equivalent to Fine-Grained Gabbro in Good et al., 2015), and the Metabasalt represents the earliest magmatism in the Coldwell Complex (Good et al., 2017). The gabbroic intrusions were grouped into two distinctive magmatic series: an older Layered Series and a younger Marathon Series. The relative ages of these units were established from crosscutting relationships, particularly within the numerous units of igneous breccia (Good et al., 2015). The Layered Series constitutes the bulk of the Eastern Gabbro and is composed of massive to mineralogically layered olivine gabbro, with a lesser amount of weakly layered oxide augite melatroctolite. The Marathon Series comprises numerous small intrusions composed predominantly of subophitic gabbro, apatitic olivine clinopyroxenite, and oxide melatroctolite, as well as small volumes of augite troctolite (Good et al., 2015).

Three Cu-Pd occurrences hosted by the Marathon Series were examined in this study. Area 41 is a Cu-Pd prospect located approximately 16 km northwest of the Marathon Cu-Pd deposit. The Area 41 intrusion is approximately 100 m thick and extends for at least 1200 m along strike (Good et al., 2017). It cuts a sequence of the Metabasalt and consists of several cross-cutting units that resemble the Two Duck Lake intrusion, the main host unit for the Marathon deposit (Good et al., 2015). Disseminated sulfide mineralization (dominantly chalcopyrite, pyrrhotite, and pyrite) occurs as three bifurcating and sub-parallel zones, predominantly within a subophitic gabbro horizon, with lesser amounts hosted by apatitic olivine clinopyroxenite. Mineralization hosted by subophitic gabbro generally has a higher Pd grade (> 1.0 ppm) than that hosted by apatitic olivine clinopyroxenite (0.1–0.8 ppm). The second area is Four Dams, approximately 2.5 km north of the Marathon deposit. It consists mainly of two mineralized occurrences: Four Dams North and Four Dams South (Fig. 3). Four Dams North consists of Cu-PGE mineralization within a 100 m-thick lens of apatitic olivine clinopyroxenite that strikes northwest for 350 m and dips 60° to the southwest (McBride, 2013). Sulfides consist of disseminated to blebby chalcopyrite with lesser amounts of pyrrhotite and trace bornite. Four Dams South consists of disseminated chalcopyrite and pyrrhotite with negligible PGE. The sulfides are hosted in mineralogically layered olivine gabbro that is continuous for 700 m along strike, dips 40°to the southwest, and varies 4 to 50 m in thicknesses (McBride, 2013). The third area is the WD zone, which is located 4 km south of the Marathon deposit. The Cu-Pd mineralization here consists of disseminated chalcopyrite and pyrrhotite and is hosted by subophitic gabbro that texturally resembles the Two Duck Lake gabbro.

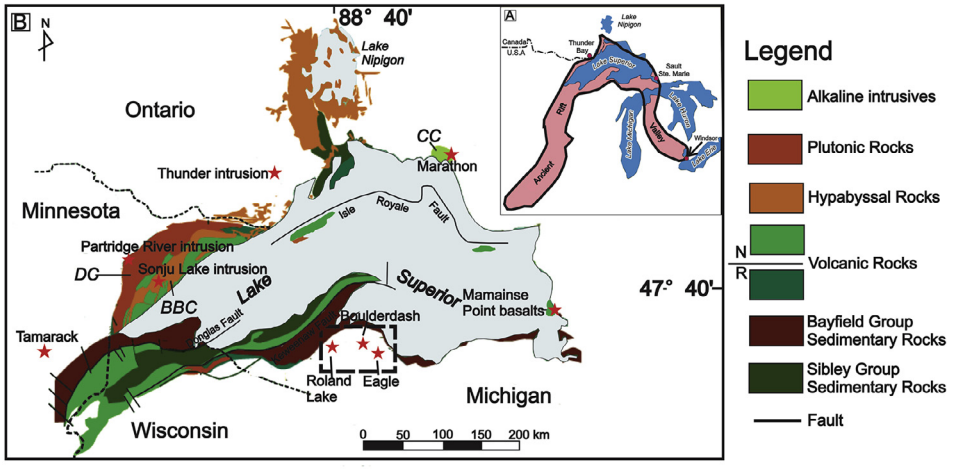

Fig. 1. (A) Extent of the Midcontinent Rift System from Van Schmus et al. (1987). (B) Locations of the Marathon deposit, the Partridge River Intrusion, the Thunder Intrusion, the Tamarack Intrusive Complex, the Sonju Lake intrusion, the Roland Lake Intrusion, the Boulderdash Intrusion, the Eagle Intrusion, and the Mamainse Point basalts (indicated as red stars) within the Midcontinent Rift (after Miller and Nicholson, 2013). The Baraga Basin Area is outlined using a dashed square. The outside area to the north of Lake Superior is Archean basement, and to the south is Phanerozoic undivided units. N/R indicates normal and reverse magnetic polarity (Miller and Nicholson, 2013). Abbreviations: DC = Duluth Complex, CC = Coldwell Complex, BBC = Beaver Bay Complex. (For interpretation of the references to colour in this figure legend, the reader is referred to the web version of this article.)

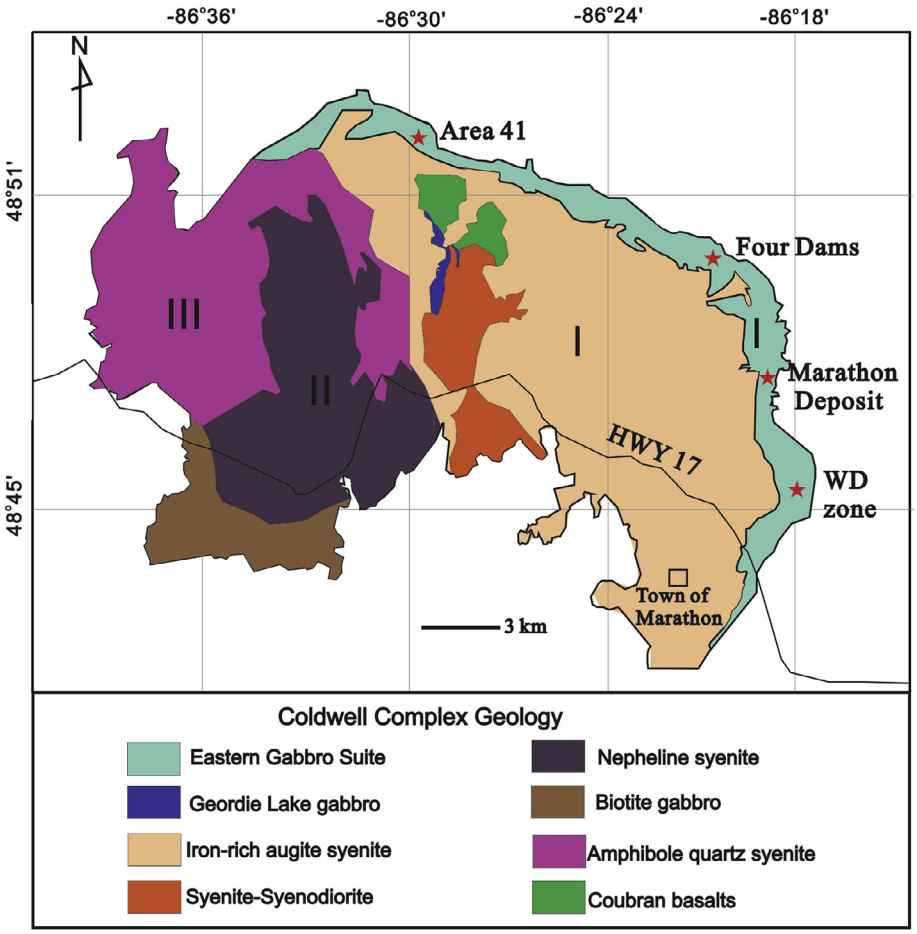

Fig. 2. Simplified geological map of the Coldwell Complex, situated on the north shore of Lake Superior (after Walker et al., 1993; Good et al., 2015). The Roman numerals I, II, and III represent intrusive centers of syenitic units in the Coldwell Complex, as described by Walker et al. (1993) and Shaw (1997). Locations of Area 41, Four Dams, the Marathon deposit, and the WD zone are represented as red stars. (For interpretation of the references to colour in this figure legend, the reader is referred to the web version of this article.)

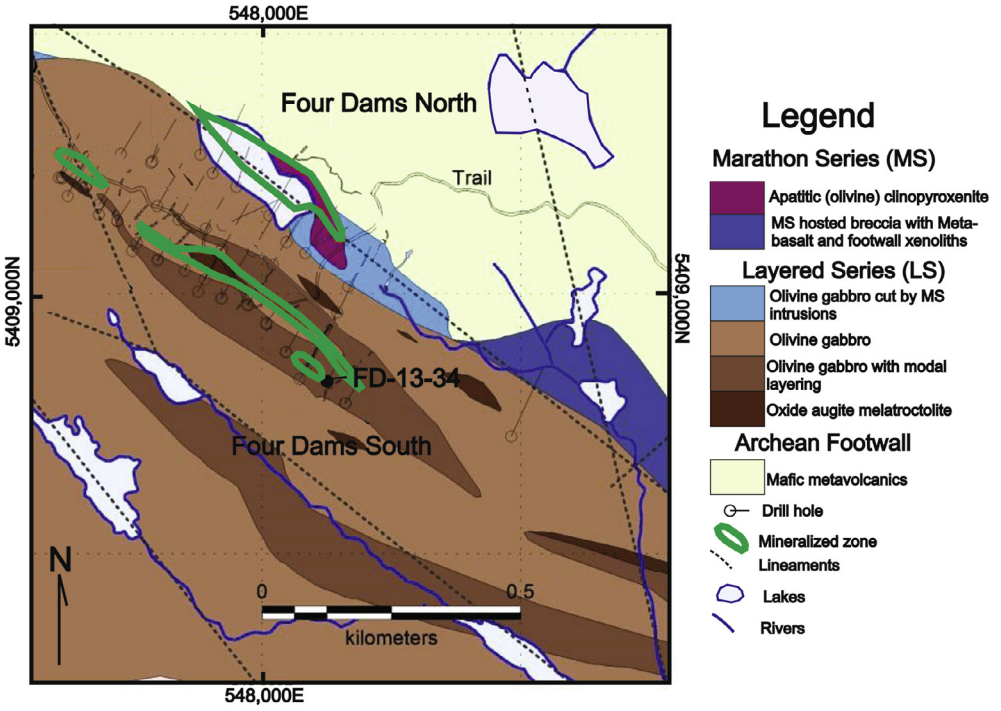

Fig. 3. The surface geology at Four Dams (modified after McBride, 2013). PGE mineralized zones projected to surface are outlined using green polygons, and the location of FD-13-34 is indicated as a black dot. The lineaments are interpreted to be normal faults with limited offsets. (For interpretation of the references to colour in this figure legend, the reader is referred to the web version of this article.)

3. Methods

3.1. Sample preparation

Powders and rock specimens were obtained from representative diamond drill holes at Area 41 (SL-13-32, SL-13-34, SL-13-37, SL-13-41), Four Dams (FD-13-34), and the WD zone (MW-07-06). A longitudinal section that displays distributions of the included Area 41 drill holes is shown in Cao (2017). All of these drill holes intersect a complete suite of Eastern Gabbro intrusive rocks.

A total of 283 powdered samples were collected by grinding 1 m-long channels at regular intervals along the length of the drill core, approximately 4 mm wide and 3 cm deep, using a Thermo Scientific portable grinder. A gap of roughly 4.5 m separated samples, and a typical sample took approximately 2 to 5 min to collect. Grain sizes of powered samples are *ca.* 10 to 200 μm. Cao et al. (2016) evaluated the influence of grain size by conducting pXRF analyses on re-ground powders, and found that for these sizes, grain size had little effect on the results. In addition, the potential contamination introduced by the grinder blade was evaluated by Cao et al. (2016) to be insignificant except for Ni, where approximately 100 ppm Ni was added into each sample during grinding. Sample locations for powdered samples are given in Fig. 4. After grinding, powders were loaded into XRF sample cups capped with 4-μm film for pXRF analyses. A subset of representative powder samples was further pulverized and sent for lab-based analyses.

A total of 149 polished thin sections, representative of different gabbro units with different styles of mineralization (e.g., chalcopyrite-rich, and pyrrhotite-rich), were prepared for petrographic and mineral chemical studies. The interval between mineralogical samples was 5 to 20 m; locations of polished thin section samples are given in Fig. 4. Note that although polished thin sections were used in this study, Cao et al. (2016) demonstrated that analyses could also be obtained from cut blocks. A comparison of results from cut blocks (unpolished and polished) and polished thin sections is provided below.

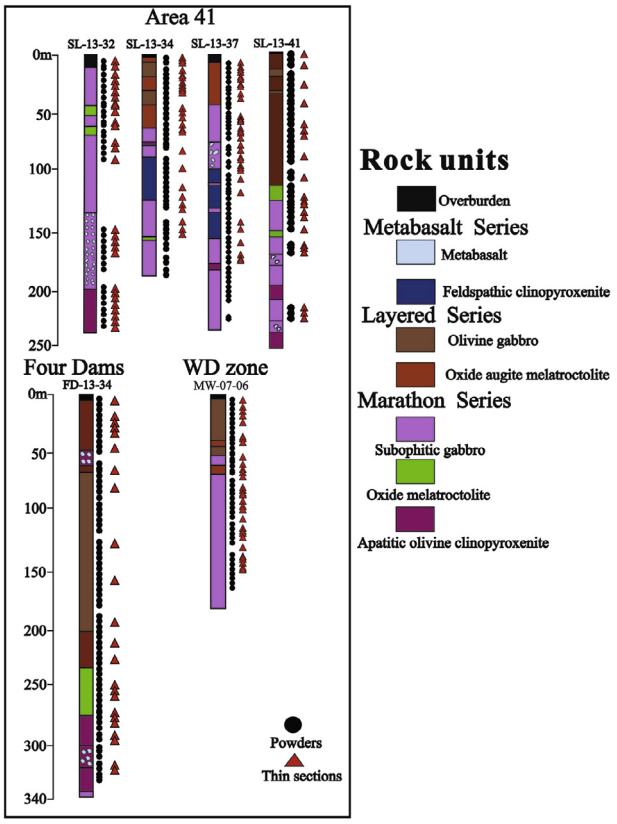

Fig. 4. Sample locations for powders (circles) and thin sections (triangles) from six representative diamond drill holes: FD-13-34 at Four Dams, SL-13-32, SL-13-34, SL-13-37 and SL-13-41 at Area 41, and MW-07-06 at the WD zone. The columns represent the geological log for each of the drill holes. The location of the Marathon Cu-Pd deposit is indicated by a red star. The small symbols in subophitic gabbro and apatitic olivine clinopyroxenite represent the Metabasalt xenoliths. (For interpretation of the references to colour in this figure legend, the reader is referred to the web version of this article.)

3.2. Analytical equipment

A NitonXL3t + GOLDD + pXRF analyzer equipped with a silicon drift detector (SDD), and a high energy, 50 kV X-ray Ag anode tube was used to analyze powdered samples. Details of analytical strategies and QA/QC control are given in Cao et al. (2016), and detection limits were provided by manufacturer. The analytical error for pXRF analysis with 95% confidence (2σ) was determined through five duplicate analyses conducted on the same sample. pXRF results with analytical errors for elements of interest (Cu, S, Ba, V, Ti) are tabulated in Tables 1 and A1. Conventional lithogeochemical analyses were conducted on selected re-ground samples by ALS Mineral Division in Vancouver. Major elements were analyzed by lithium borate fusion and inductively coupled plasma (ICP)-atomic emission spectroscopy (AES) on a minimum 2 g of pulp samples. Trace elements were analyzed by lithium borate fusion and ICP-mass spectroscopy (MS) on 2 g of pulp samples. Total S was determined using a Leco combustion furnace on 0.01 to 0.1 g of sample, in which the sample is heated to roughly 1350 °C in an induction furnace. SO_2 is produced through reaction with oxygen and is measured by an infra-red detector. Quality control was achieved using ALS geochemical quality-control procedures, which involve analyses on a wide array of standards, blanks, and duplicates after each batch of samples. Representative conventional lithogeochemical results with 95% confidence (2σ standard deviation) are given in Table 1.

Major constituents of olivine, clinopyroxene, and plagioclase were acquired on a JEOL JCM-6000 NeoScope SEM (bSEM) equipped with a JEOL JED-2300 energy-dispersive X-ray analyzer at Western University. Carbon-coated polished thin sections were analyzed using 15 keV accelerating voltage, a high beam current, a 19 mm working distance, a 30–40 μm beam size, and standardless ZAF corrections. Cao et al. (2016) evaluated the analytical precision of bSEM-EDS analyses by analyzing the same spot 10 times: results are ± 0.51 for the Mg# (molar Mg/(Mg + Fe)*100) of olivine, ± 1.0 for the Mg# of clinopyroxene, and ± 0.63 for the anorthite content (molar Ca/(Ca + Na)*100) of plagioclase (1σ standard deviation). The analytical precision (machine error), combining with the nature variation, constitute the sample variability determined through bSEM-EDS analyses on 3–5 grains of each mineral type in each sample (Tables 2 and A2). A subset of representative carbon-coated polished thin sections was chosen for electron microprobe analyses, conducted using a JEOL JXA-8530F field-emission probe at Western University. Major and minor constituents of olivine (Mg, Fe, Si), plagioclase (Na, Ca, Al, Si), clinopyroxene (Mg, Ca, Fe, Si) were measured. Detection limits for these elements are typically down to ~100 ppm and no peak overlapping corrections were needed. The operating conditions were an accelerating voltage of 15 keV and a beam current of 20nA, a 1 μm spot size for analyzing olivine and clinopyroxene, and a 5 μm spot size for analyzing plagioclase. The peak and background counting time was 30 s for all elements. A variety of synthetic and natural standards were used to calibrate different elements during probe analyses. The precision of electron microprobe analyses was determined by Cao et al. (2016) to be ± 0.07 for Mg# of olivine, ± 0.30 for Mg# of clinopyroxene, and ± 0.15 for plagioclase anorthite content (1σ standard deviation), determined by analysis of the same spot 10 times. These values (machine errors) are significantly lower than those for EDS analyses, and are also well below the sample variabilities which were determined through bSEM-EDS analyses of 3 to 5 grains of each mineral type

Table 1
Selected lab-based and pXRF whole-rock Ba, Cu, S, V, Ti concentrations, and ratios of V/Ti and Cu/S in this study. 95% confidence error for element is given in bracket, error for the ratio represents 95% confidence error calculated based on the equation $\sigma_{(A/B)} = A/B \times ((\sigma_A/A)^2 + (\sigma_B/B)^2)^{1/2}$. Abbreviations: LS = Layered Series, MS = Marathon Series, OAM = oxide augite melatroctolite, OG = olivine gabbro, SG = subophitic gabbro.

Drill hole	Depth/m	Series	Unit	pXRF Ti (0.024)	Lab-based Ti (0.018)	pXRF Cu (44)	Lab-based Cu (10.3)	pXRF S (200)	Lab-based S (60)	pXRF V (22)	Lab-based V (17.5)
SL-13-32	17	MS	SG	1.47	1.34	2662	3340	11,680	15,300	463	383
	32		SG	1.35	1.35	2443	3980	5970	8400	433	434
	37		SG	1.58	1.45	333	414		1400	560	468
MW-07-06	3.9	LS	OG	1.58	1.60	208	258		2000	215	121
	7.9		OG	1.64	0.00	151				177	
	11.9		OG	2.50	2.42	114	119		2000	326	176
	15.9		OG	2.14	0.00	91		629		234	
	19.9		OG	2.08	1.96	119	124		1800	306	194
	23.9		OG	1.83	1.79	123	126		1900	309	201
	38		OAM	2.70	2.37	113	118		1200	410	278
	80.6	MS	SG	1.19	1.22	76	69	725	2000	139	83
	91.5		SG	2.45	2.38	255	300	1017	2600	245	116
	95.5		SG	3.58	3.32	651	742	2751	5000	481	282
	109.5		SG	3.20	3.07	1794	2310	3488	4300	1135	1110
	113.5		SG	2.46	2.19	638	653		1000	1179	1030
	117.5		SG	2.53	2.42	1009	1145		1800	1229	1220
	121		SG	2.02	1.92	1135	1225		1300	1085	1000
	135.5		SG	2.50	2.29	625	696		700	1505	1400
	143.5		SG	3.33	3.27	230	222	12,353	15,600	559	344
	147.5		SG	1.89	1.77	1450	2100		2200	954	899
SL-13-32	17	999	1130	0.03	0.002	0.03	0.001	0.23	0.005	0.22	0.001
	32	828	942	0.03	0.002	0.03	0.001	0.41	0.016	0.47	0.004
	37	725	785	0.04	0.002	0.03	0.001			0.30	0.015
MW-07-06	3.9		10,000	0.01	0.001	0.01	0.001			0.13	0.006
	7.9			0.01	0.001						
	11.9	5540	7000	0.01	0.001	0.01	0.001			0.06	0.006
	15.9	4636		0.01	0.001			0.15	0.084		
	19.9	2989	4140	0.02	0.001	0.01	0.001			0.07	0.006
	23.9	2672	3510	0.02	0.001	0.01	0.001			0.07	0.006
	38	1980	2440	0.02	0.001	0.01	0.001			0.10	0.010
	80.6	1254	1705	0.01	0.002	0.01	0.001	0.11	0.067	0.04	0.005
	91.5	1053	1430	0.01	0.001	0.01	0.001	0.25	0.066	0.12	0.005
	95.5	812	835	0.01	0.001	0.01	0.001	0.24	0.024	0.15	0.003
	109.5	539	505	0.04	0.001	0.04	0.001	0.51	0.032	0.54	0.008
	113.5	390	314	0.05	0.001	0.05	0.001			0.65	0.041
	117.5	362	272	0.05	0.001	0.05	0.001			0.64	0.022
	121	541	515	0.05	0.001	0.05	0.001			0.94	0.044
	135.5	368	239	0.06	0.001	0.06	0.001			0.99	0.087
	143.5		4	0.02	0.001	0.01	0.001	0.02	0.004	0.01	0.001
	147.5	318	284	0.05	0.001	0.05	0.001			0.96	0.027

(Tables 2 and A2).

Fig. 5 compares bSEM-EDS analytical results and images for a sample prepared in three ways: an unpolished cut thin section block; a polished cut thin section block, and; a carbon-coated polished thin section. The analytical results from the unpolished block and polished block are similar to those from the polished thin section, and the polishing process for the block improved the results to some extent, i.e., compared to results from the unpolished block, results from the polished block are closer to the results from the polished thin section. BSE images and EDS mapping for all three sample preparations are similar in terms of identifying minerals and textures, although the rough surface is evident on the BSE image from the unpolished block.

4. Lithology

4.1. Metabasalt

The Metabasalt was intruded by the Marathon Series and occurs locally as xenoliths within the Marathon Series rocks. Its composition varies from basalt to olivine basalt, and consists of equigranular, fine-grained subhedral clinopyroxene, olivine, and magnetite, with interstitial plagioclase. The Metabasalt is distinguished by its recrystallized texture (120° boundaries between crystals, Fig. 6A), reflecting the pyroxene hornfels-grade metamorphism, likely caused by heat from later intrusions.

4.2. Feldspathic clinopyroxenite

The feldspathic clinopyroxenite is exposed at Area 41, but is not observed at either Four Dams or in the WD zone. Based on crosscutting relationships and mineral textures, McBride (2013) suggested that the feldspathic clinopyroxenite is an older intrusion that is potentially co-genetic with the Metabasalt. It consists of medium-to coarse-grained subhedral clinopyroxene (60–80 modal %), subhedral olivine (5–15 modal %), anhedral plagioclase (5–10 modal %), magnetite (< 5 modal %), and trace disseminated pyrrhotite and chalcopyrite. Plagioclase occurs as anhedral grains interstitial to subhedral olivine and subhedral clinopyroxene. Magnetite and sulfide minerals typically occur as inclusions within olivine and clinopyroxene. The feldspathic clinopyroxenite is weakly altered, as reflected by a network of thin chlorite stringers in olivine (Fig. 6B).

4.3. Olivine gabbro and oxide augite melatroctolite

Olivine gabbro is medium- to coarse-grained (1–4 mm). Layering of this unit is defined by a gradational change in the abundance of plagioclase relative to the abundances of clinopyroxene and magnetite (Fig. 7A). It consists of euhedral plagioclase (40–60 modal %), subhedral clinopyroxene (15–30 modal %), subhedral olivine (10–15 modal %), less than 10 modal % apatite plus magnetite, and less than 5

Table 2
Selected Mg# values of olivine and clinopyroxene, and the anorthite content of plagioclase determined by bSEM-EDS and electron microprobe. St. dev refers to 1 σ standard deviation determined on multiple analyses on 3–5 grains of each mineral type in each sample. Abbreviations: LS = Layered Series, MS = Marathon Series, OAM = oxide augite melatroctolite, OG = olivine gabbro.

Drill hole	Depth/m	Series	Unit	Mg# of olivine				Mg# of clinopyroxene				Anorthite content of plagioclase			
				Probe	St.dev	bSEM-EDS	St.dev	Probe	St.dev	bSEM-EDS	St.dev	Probe	St.dev	bSEM-EDS	St.dev
SL-13-34	3	LS	OAM	37	1.5	49	1.2	67	1.3	77	0.8	54	1.9	53	3.6
	5.1		OAM	33	0.3	40	1.6	67	1	72	1.2	52	1.7	52	1.2
	7		OG	35	1.0	42	1.1	66	1.2	70	2.5	52	0.6	51	0.6
	13.3		OG	32	0.5	42	3	68	1.2	73	1.1	51	0.8	54	6.5
	17.4		OG	38	1.3	44	1.2	67	1.6	72	2.0	52	1.0	52	1.2
	19.4		OAM	42	0.2	46	0.7	67	0.6	70	0.8	52	0.4	55	2.3
	25.7		OAM	42	0.6	53	1.2	68	0.4	75	2.5	53	2.5	52	1.2
	28.1		OAM	44	2.0	50	1.5	68	0.6	74	0.8				
	30		OAM	48	1.3	54	1.5	68	0.3	74	1.0	52	0.6	52	1.2
	32		OG	42	1.1	51	1.6	68	0.6	76	0.7	54	1.0	49	2.2
	45		OG	47	0.4	55	1.2	69	0.5	76	1.2	55	2.4	52	1.2
	49		OAM	48	1.5	56	0.8	68	0.6	76	0.6	56	0.5	53	2.1
	53		OAM	51	0.3	60	1.2	70	0.3	77	0.8	57	1.0	52	1.2
	58.9		OAM	49	0.4	54	1.3	70	0.4	74	1.2	56	0.9	55	2.4
SL-13-41	3	LS	OAM	28	0.5	33	1.0	60	1.1	63	0.8	43	2.1	29	1.9
	7.5		OAM	24	0.9			56	1.7			24	0.7		
	12.1		OAM	36	0.2	45	0.7	69	0.1	78	3.2	53	1.3	45	2.4
	45		OAM	38	0.5	54	1.3	65	1.1	79	1.2	54	2.0	44	1.7
	63.2		OAM	44	0.2	62	1.5	68	0.4	83	0.8	52	1.5	48	2.4
	68.9		OAM	46	0.2	66	1.2	68	0.8	78	1.5	51	0.6	41	1.2
	73		OAM	51	0.2	68	1.5	69	0.3	81	3.3	56	0.6	44	2.1
	91		OAM	53	0.5	62	1.3	71	0.9	76	1.0	55	0.2	47	3.4
	109.1		OAM	57	0.2	73	0.7	71	0.4	82	0.6	55	1.4	44	2.2

modal % subhedral biotite and/or anhedral alkali feldspar. Plagioclase grains locally occur as chadocrysts enclosed by olivine and clinopyroxene oikocrysts, and olivine locally is rimed by clinopyroxene. Minor phases such as apatite and magnetite typically occur within, or locally interstitial to, olivine and plagioclase. Biotite occurs interstitial to olivine and plagioclase. Alkali feldspar (perthite) is common in olivine gabbro at Area 41 and the WD zone (Fig. 6C), whereas it is negligible in olivine gabbro at Four Dams (Cao et al., 2016). Locally, olivine gabbro grades into discontinuous lenses of weakly layered oxide augite melatroctolite that is distinguished by abundant magnetite (10 to 20 modal %) and higher amounts of olivine (20–45 modal %) and clinopyroxene (10–20 modal %) than in the olivine gabbro. Cao (2017) concluded that olivine gabbro and oxide augite melatroctolite are geochemically similar units, and that their differences in mineral abundances are a result of crystal sorting, possibly caused by mass slumping in the magma chamber.

4.4. Subophitic gabbro

Subophitic gabbro is medium- to coarse-grained (< 8 mm) to pegmatitic (> 2 cm). It has a characteristic subophitic texture for clinopyroxene and subhedral plagioclase that resembles the Two Duck Lake gabbro at the Marathon deposit (Fig. 7B). It consists of subhedral plagioclase (40–70 modal %), euhedral to subhedral olivine (5–10 modal

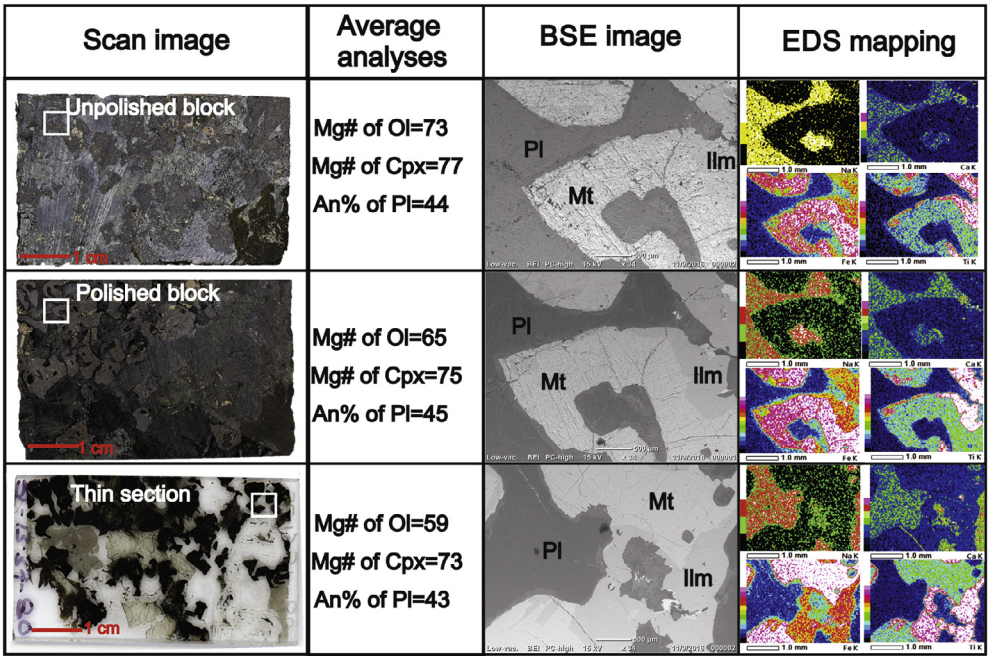

Fig. 5. Comparison of EDS results, BSE images, and EDS mappings for the same sample (SL-13-37-80) prepared by three different methods: unpolished cut thin section block, polished cut thin section block, and carbon-coated thin section. The white square denotes the location for BSE image. Abbreviations: Ol = olivine, Cpx = clinopyroxene, Pl = plagioclase, Mt = magnetite, Ilm = ilmenite.

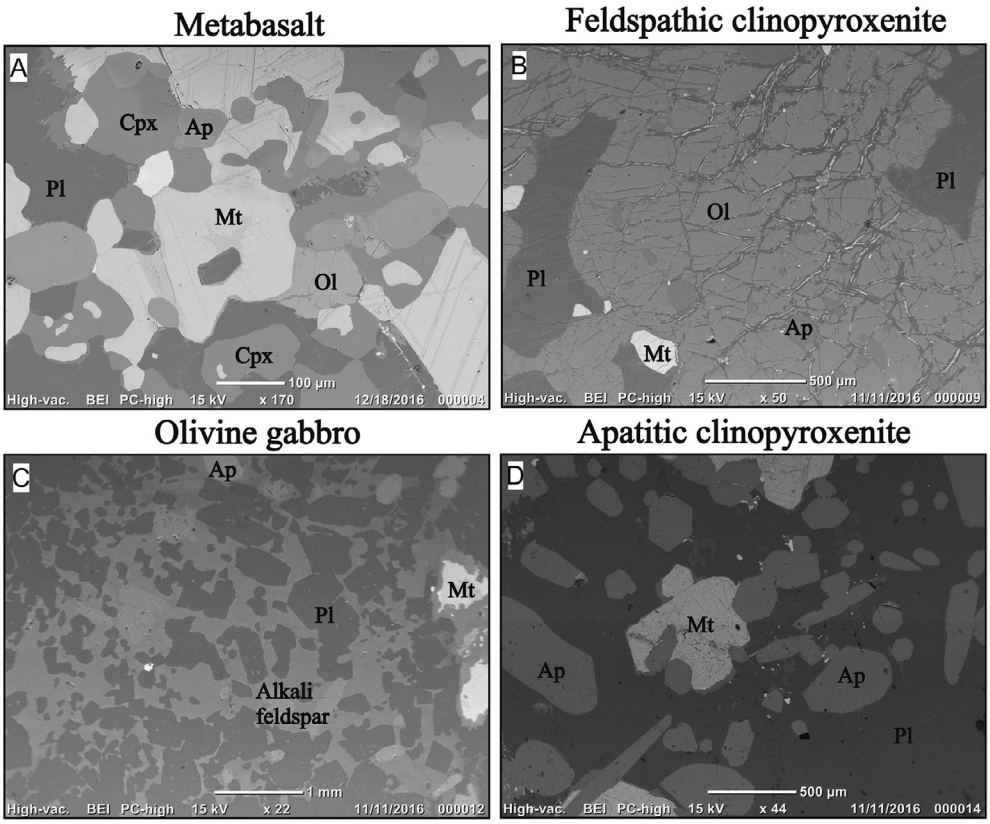

Fig. 6. Benchtop SEM images of polished thin sections. BSE images show mineral compositions and textures for various units. (A) The recrystallized texture observed in the Metabasalt, note the nearly 120° angles of boundaries between different crystals. (B) The net-work of chlorite stingers cross-cutting an olivine crystal, observed in feldspathic clinopyroxenite. (C) Alkali feldspar surrounds euhedral-subhedral plagioclase in olivine gabbro at Area 41. (D) Apatite inclusions in plagioclase, observed in apatitic olivine clinopyroxenite.

%), anhedral clinopyroxene (15–30 modal %), and minor interstitial magnetite and apatite (< 10 modal %). This unit is the main host of Cu-PGE mineralization at both Area 41 and the WD zone. However, at Four Dams, only a small amount of subophitic gabbro is present. At Area 41, subophitic gabbro can be further subdivided into three subtypes based on differences in grain size, namely medium-grained subophitic gabbro, coarse-grained subophitic gabbro, and pegmatitic subophitic gabbro. The medium-grained subophitic gabbro contains negligible olivine, and PGE mineralization is mainly hosted by coarse-grained and pegmatitic subophitic gabbro (Cao, 2017). There is some local development of secondary minerals such as chlorite, amphibole, serpentine, and calcite, particularly in pegmatitic subophitic gabbro.

4.5. Apatitic olivine clinopyroxenite

Apatitic olivine clinopyroxenite is a medium- to- coarse-grained apatite-rich (up to 30 modal % apatite, Fig. 6D) cumulate rock that contains 30–60 modal % subhedral clinopyroxene, 10–20 modal % subhedral olivine, 5–10 modal % subhedral plagioclase, and less than 10 modal % magnetite and biotite. At Four Dams, this unit is the dominant host for Cu-PGE mineralization. At Area 41, apatitic olivine clinopyroxenite constitutes a minor proportion of the Marathon Series and typically occurs as thin lenses within subophitic gabbro. Chlorite and actinolite alteration is commonly observed in this unit.

4.6. Oxide melatroctolite

Oxide melatroctolite occurs as small pods and sills that are typically located within the main body of subophitic gabbro at Area 41 and the WD zone. At the Four Dams area, this unit sits below oxide augite melatroctolite, and constitutes an important marker horizon that indicates the transition from the Layered Series to the Marathon Series (Cao et al., 2016). This unit contains significant subhedral magnetite (40–60 modal %), less than 30 modal % subhedral olivine and plagioclase, and minor amounts of subhedral clinopyroxene and euhedral apatite.

5. Validation of results from portable techniques

Since the accuracy and precision of data collected by field portable analytical instruments are inevitably poorer than those of lab-based analyses (Cao et al., 2016), appropriate quality assurance procedures

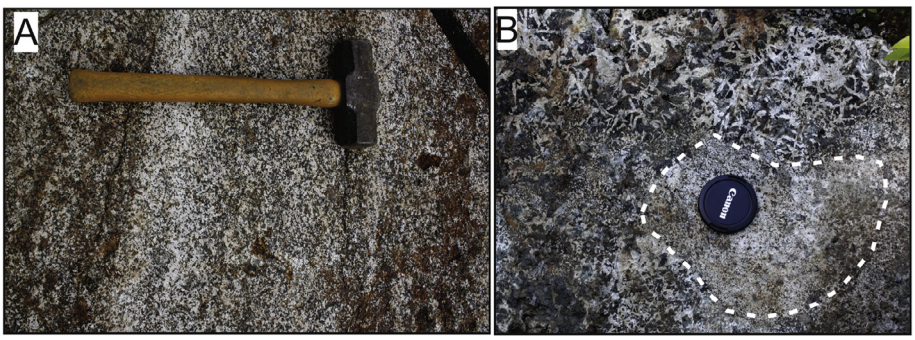

Fig. 7. Outcrop pictures for the Layered Series units and the Marathon Series subophitic gabbro. (A) The layering reflects a gradational change in the abundance of plagioclase relative to the abundances of clinopyroxene and magnetite. (B) Subophitic gabbro; note the typical subophitic texture for gabbro along the upper part of the photo and the finer grained xenolith (outlined by the white dotted circle) underneath the lens cap.

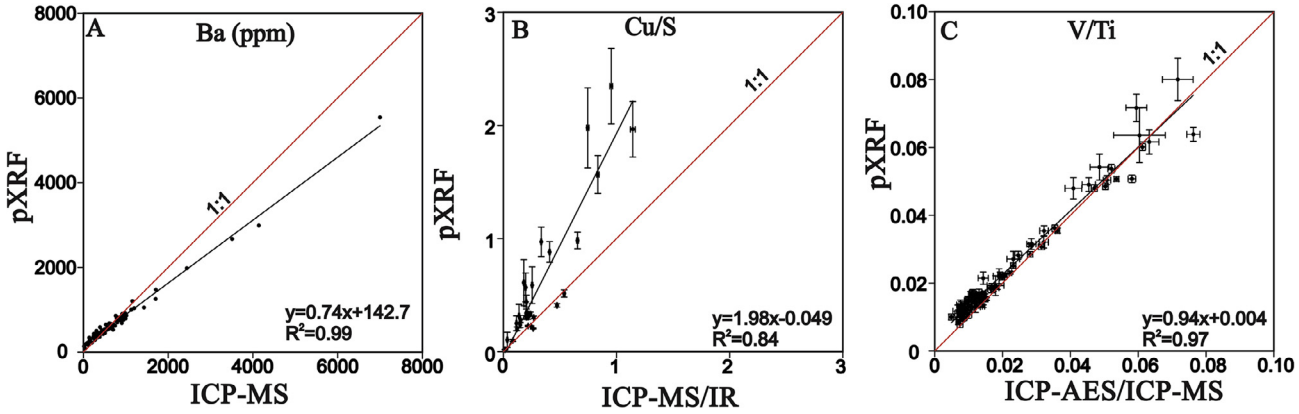

Fig. 8. Comparisons between pXRF analyses and ICP-AES/ICP-MS/IR analyses for Ba (A), Cu/S (B), and V/Ti (C). Error bar represents 95% confidence (2σ standard deviation) of analytical uncertainty determined by repetitive analyses. The error in Fig. 8A is smaller than the symbol.

should be assessed prior to interpretation.

5.1. pXRF

pXRF analyses of Ba, Cu/S, and V/Ti are compared to their lab-based counterparts in Fig. 8. Correlation coefficients (R^2) between pXRF and ICP-AES or ICP-MS/IR are above 0.8, indicating a high degree of correlation for results between these different methods. The high accuracy of pXRF V/Ti data is reflected by data distributions that fall close to the 1:1 line with lab-based data. By contrast, pXRF data for Ba and Cu/S are less accurate. However, since there are very good correlations between pXRF and lab-based Ba and Cu/S, i.e., pXRF data have a high precision, further corrections can be applied to improve data accuracy, as shown by Cao et al. (2016). Similar data quality from pXRF has also been reported previously by Hall et al. (2014), Piercey and Devine (2014), Ross et al. (2014), and Ryan et al. (2017).

5.2. bSEM-EDS

Fig. 9 compares bSEM-EDS analyses of the Mg# of olivine, the Mg# of clinopyroxene, and the anorthite content of plagioclase with the same grains analyzed by electron microprobe. The correlation between data from the two methods are excellent for the Mg# of olivine (R^2 = 0.92) and the anorthite content of plagioclase (R^2 = 0.86), and reasonably good for the Mg# of clinopyroxene (R^2 = 0.73), similar to the comparison made by Cao et al. (2016). Therefore, down-hole variations in these parameters from bSEM-EDS analyses are comparable to their microprobe counterparts.

6. Results

6.1. pXRF whole-rock compositions

Whole-rock Ba concentrations and the V/Ti weight ratio from pXRF measurements of the different units at the three localities are shown in Fig. 10. Generally, the Ba contents of olivine gabbro and oxide augite melatroctolite are higher than those in subophitic gabbro and apatitic olivine clinopyroxenite. This is particularly evident by comparing various rock units from the same area. V/Ti ratios for olivine gabbro and oxide augite melatroctolite from all three localities are lower than 0.025, whereas those for subophitic gabbro and apatitic olivine clinopyroxenite generally are above 0.03, up to around 0.09 for apatitic olivine clinopyroxenite at Four Dams.

The whole-rock Ba and V/Ti contents of different rock types are compared in Fig. 11. The ranges for the Metabasalt, Layered, and Marathon Series rocks at the Marathon deposit are outlined using data from Good et al. (2015). Most feldspathic clinopyroxenite samples at Area 41 plot within the Metabasalt field of Good et al. (2015), supporting the suggestion of McBride (2013) that feldspathic clinopyroxenite is cogenetic with the Metabasalt. Olivine gabbro and oxide augite melatroctolite samples from Area 41, WD zone, and the Four Dams area are all within the range of the Layered Series of Good et al. (2015), whereas most of subophitic gabbro and apatitic olivine clinopyroxenite samples are within the range of the Marathon Series of Good et al. (2015).

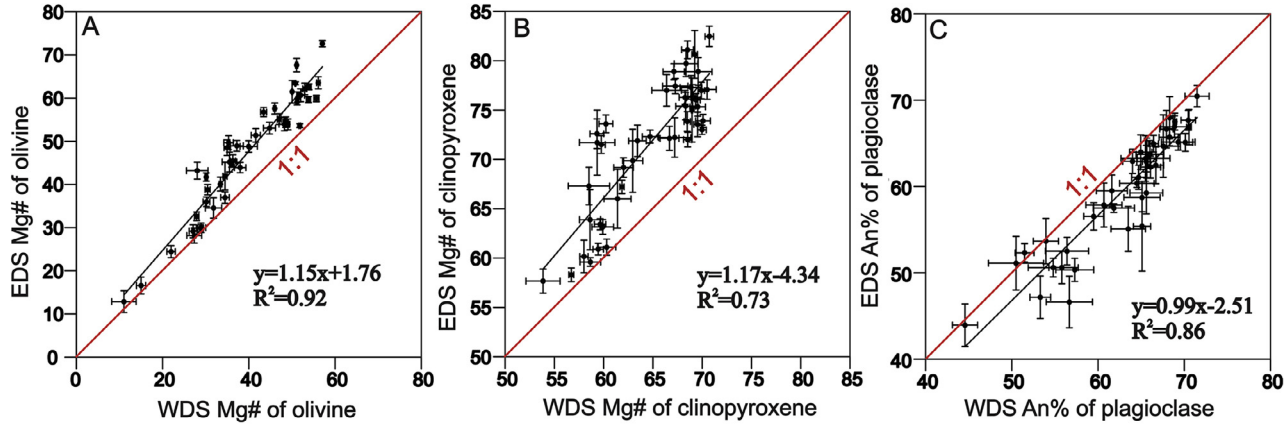

Fig. 9. Binary diagrams correlating values of the Mg# of olivine (A), the Mg# of clinopyroxene (B), and the anorthite content of plagioclase (C) determined by bSEM-EDS and electron microprobe, respectively. Error bars represent 1σ sample errors determined through EDS analyses conducted on 3 or 4 grains of each mineral type in each sample, and multiple spot analyses were conducted on each mineral grain. Average values are correlated in this figure.

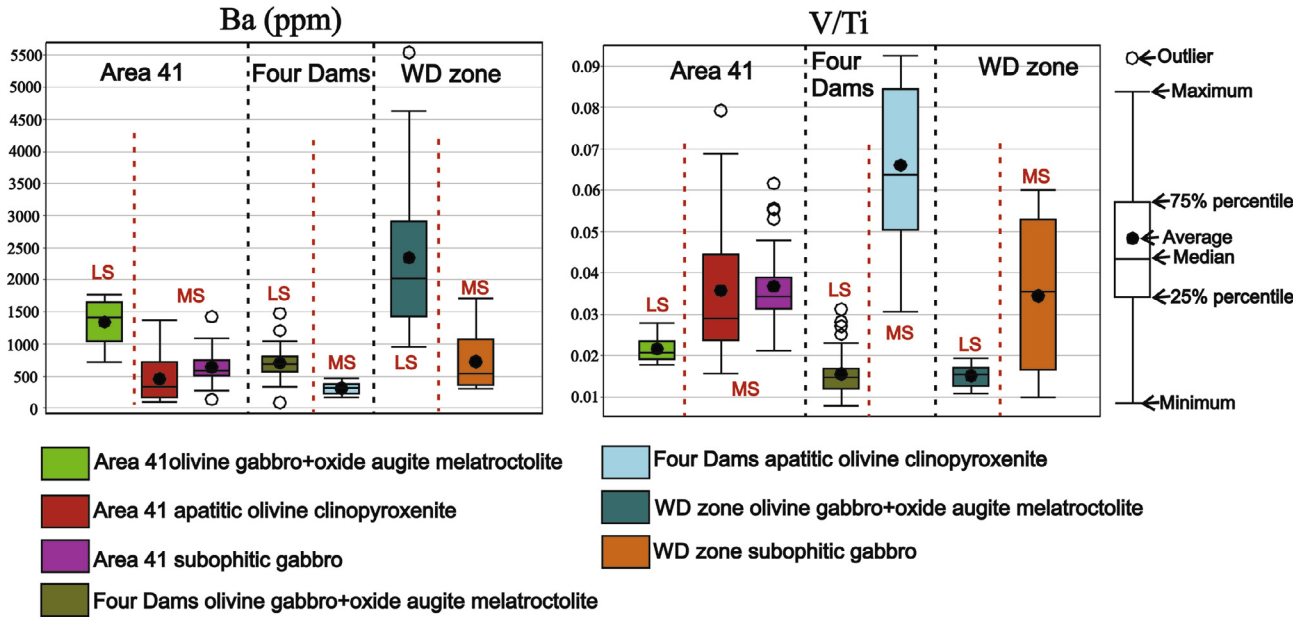

Fig. 10. Box and whisker plots for selected pXRF parameters for different rock units of different localities. Abbreviations: LS = Layered Series, MS = Marathon Series.

6.2. bSEM-EDS mineral chemical compositions

The Mg# of olivine and clinopyroxene, and the anorthite content of plagioclase determined by bSEM-EDS for various rock units are summarized in Fig. 12. The data present an excellent example of how stratigraphy can be established using bSEM-EDS. The Mg# values for olivine and clinopyroxene from apatitic olivine clinopyroxenite and subophitic gabbro are higher than those of olivine gabbro and oxide augite melatroctolite, particularly where rock units from the same area are compared. Subophitic gabbro at Area 41 and the WD zone and apatitic olivine clinopyroxenite at Four Dams also have higher anorthite contents in plagioclase than olivine gabbro and oxide augite melatroctolite. However, apatitic olivine clinopyroxenite at Area 41 has lower anorthite contents in plagioclase than olivine gabbro and oxide augite melatroctolite.

6.3. Down-hole geochemical profiles

Down-hole geochemical profiles of Cu/S (pXRF-based and/or lab-based), pXRF Ba and V/Ti, and the bSEM-EDS Mg# of olivine and clinopyroxene for three representative drill holes at Area 41 (SL-13-37), Four Dams (FD-13-34), and the WD zone (MW-07-06) are displayed in Figs. 13–15, respectively. Note that three mineralized zones (defined by > 100 ppb Pd plus Pt) are outlined in the three figures. Based on unpublished exploration assay data, the mineralized zones in SL-13-37 and FD-13-34 contain higher average PGE grades than in MW-07-06 (430 ppb Pt and 630 ppb Pd for SL-13-37, 223 ppb Pt and 400 ppb Pd for FD-13-34, and 150 ppb Pt and 390 ppb Pd for MW-07–06). Six significant characteristics of these down-hole profiles are: 1) the Ba contents in olivine gabbro and oxide augite melatroctolite at Area 41 and the WD zone generally decrease down-hole, and the V/Ti and the Mg# of olivine and clinopyroxene increase, 2) Ba and V/Ti in olivine gabbro and oxide augite melatroctolite at Four Dams are fairly constant with depth, but the Mg# of olivine and clinopyroxene decrease down-hole, 3) subophitic gabbro at Area 41 and the WD zone, by contrast, lack any consistent down-hole variations in these variables, and instead are characterized by fluctuations of these parameters, 4) V/Ti and the Mg# of olivine and clinopyroxene in the apatitic olivine clinopyroxenite at

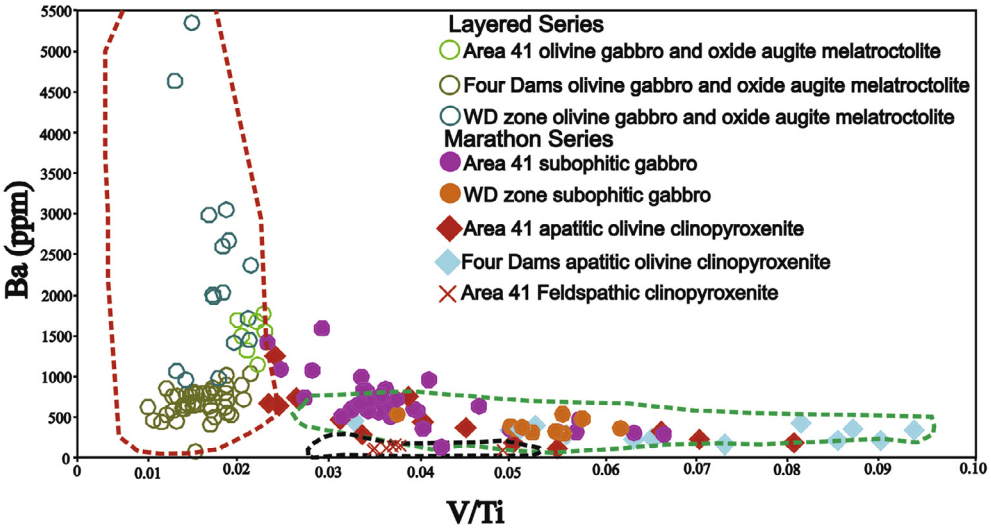

Fig. 11. The discrimination diagram of pXRF whole-rock Ba vs. V/Ti that separates different rock units in different areas of the Eastern Gabbro. For error bars see Fig. 8. The red, green, and black dashed lines outline ranges for the Layered Series, the Marathon Series, and the Metabasalt, respectively, at the Marathon deposit, using data of Good et al. (2015). (For interpretation of the references to colour in this figure legend, the reader is referred to the web version of this article.)

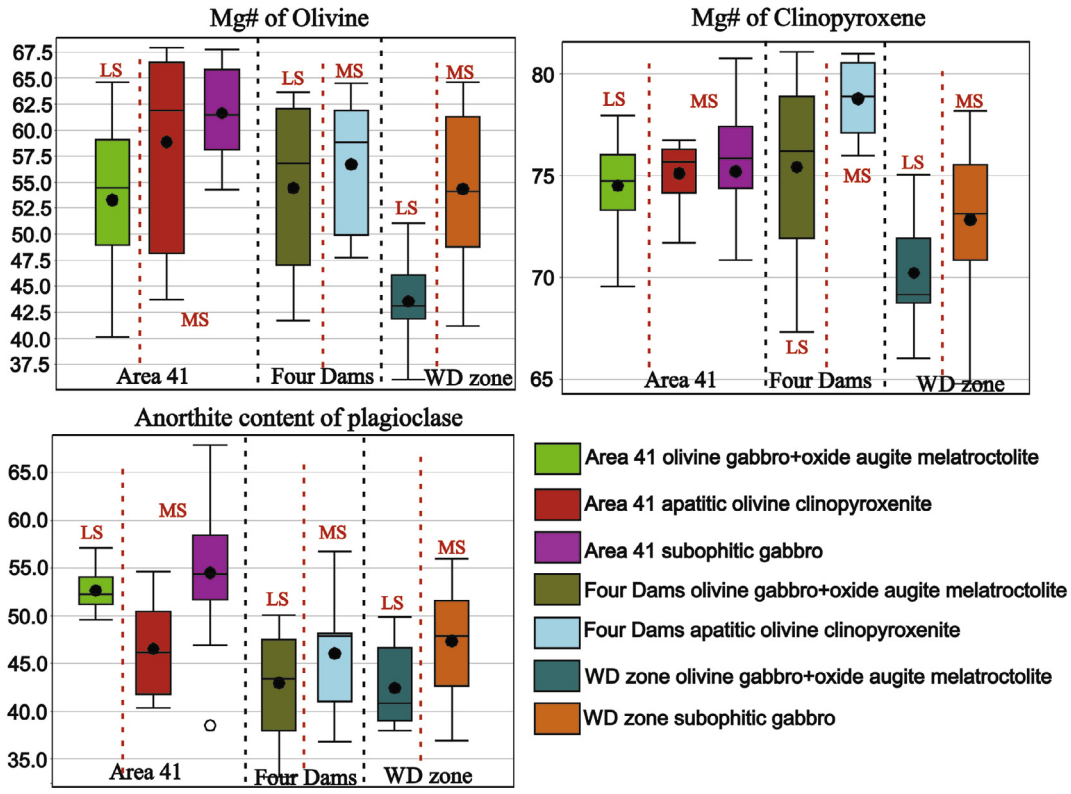

Fig. 12. Box and whisker plots for mineral chemical compositions determined by bSEM-EDS on polished thin sections for different rock units at each locality. Abbreviations: LS = Layered Series, MS = Marathon Series.

Four Dams generally increase down-hole, but all of these variables also show fluctuations, 5) rock units within the PGE mineralized zones in the shown drill holes contain significantly higher Cu/S ratios than other rock units, and 6) in SL-13-37, Mg# values for olivine and clinopyroxene from PGE mineralized subophitic gabbro show greater variability than crystals from olivine gabbro and oxide augite melatroctolite, as well as from the other PGE-poor subophitic gabbro rocks (see error bars in Fig. 13). Note that other drill holes (see Tables A1 and A2) exhibit similar characteristics to those illustrated above.

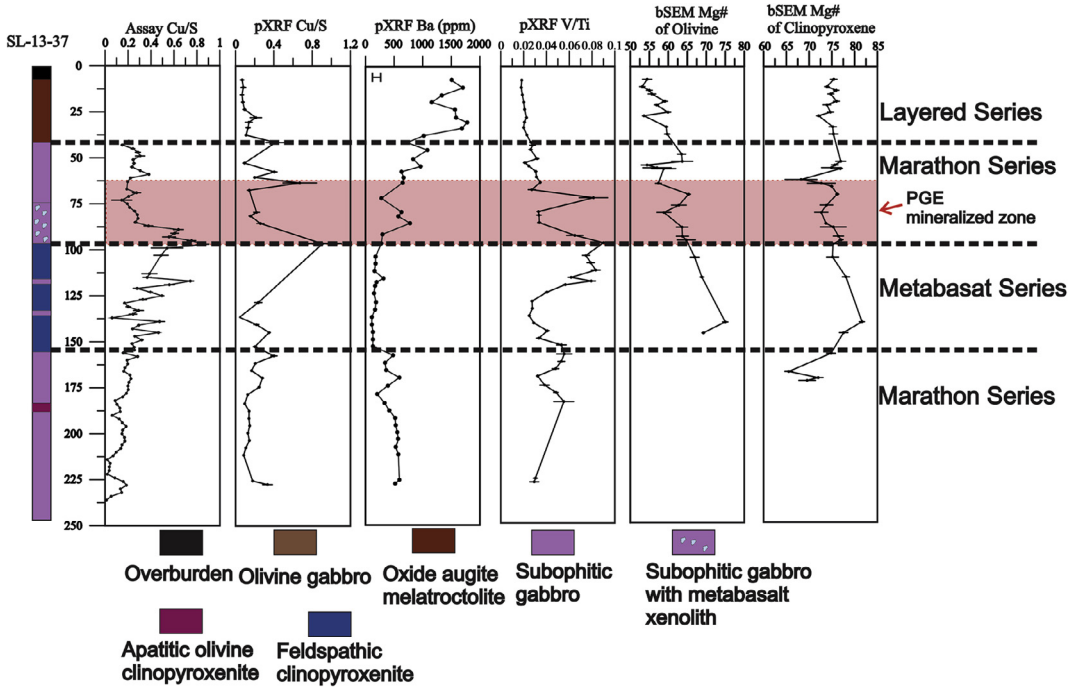

Fig. 13. pXRF, bSEM-EDS, and lab assay geochemical profiles down the drill hole SL-13-37 at Area 41, the shaded area indicates the disseminated Cu-PGE mineralized zone. The error bar for pXRF analysis represents 2σ analytical uncertainty determined by multiple analyses on the same powder. The error bar for bSEM-EDS analysis represents 1σ sample variability determined by 3–5 analyses on 3–5 grains of each mineral type in each sample.

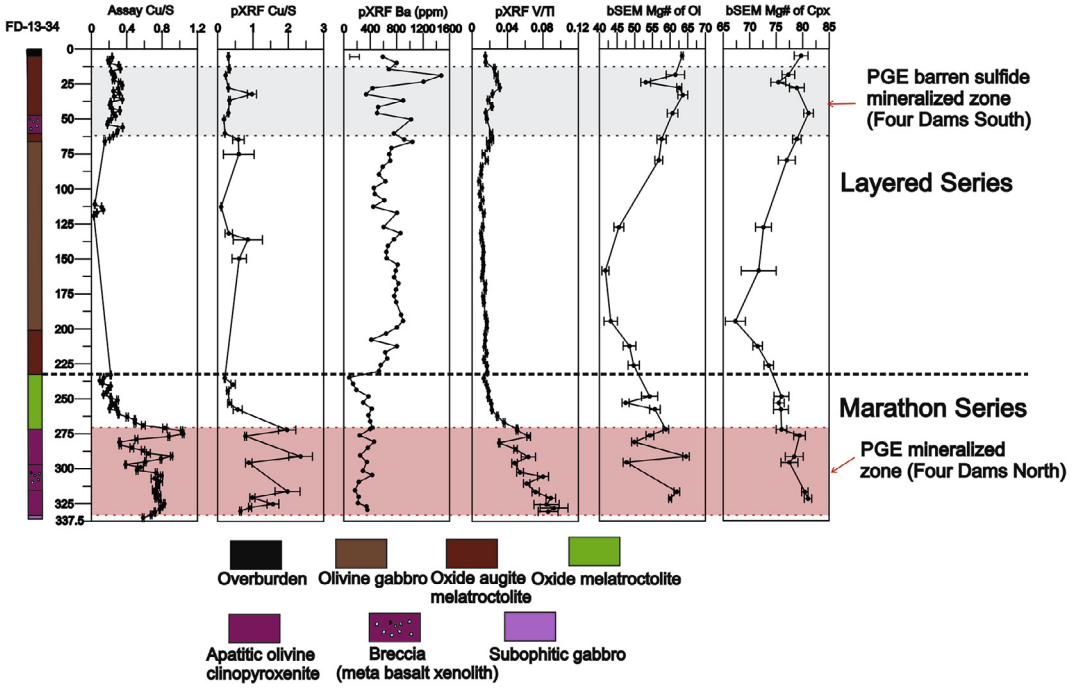

Fig. 14. pXRF, bSEM-EDS, and lab assay geochemical profiles down the drill hole FD-13-34 at Four Dams, the pink shaded area indicates the Four Dams North disseminated Cu-PGE mineralized zone and the grey shaded area indicates the Four Dams South mineralized zone. The error bar for pXRF analysis represents 2σ analytical uncertainty determined by multiple analyses on the same powder. The error bar for bSEM-EDS analysis represents 1σ sample variability determined by 3–5 analyses on 3–5 grains of each mineral type in each sample. (For interpretation of the references to colour in this figure legend, the reader is referred to the web version of this article.)

7. Discussion

7.1. Discriminating between barren and mineralized intrusive rocks

The pXRF results show that olivine gabbro and oxide augite melatroctolite have higher whole-rock Ba contents and lower V/Ti ratios compared to subophitic gabbro and apatitic olivine clinopyroxenite (Figs. 10 and 11). Shaw (1997) and Cao et al. (2016) relate the differences in the Ba contents of these two series to the greater abundance of Ba-rich biotite and orthoclase in the Layered Series. The lower V/Ti ratio of the Layered Series may indicate that it is more evolved than the Marathon Series because down-hole V/Ti and mineral compositional profiles in the same holes in the Layered Series (Figs. 13 and 15) suggest that V is more compatible than Ti in this magmatic system, i.e., V has a higher bulk partition coefficient than Ti due to the fractionation of clinopyroxene, magnetite, etc. This is consistent with the generally lower Mg# values of the olivine and clinopyroxene in the olivine gabbro and oxide augite melatroctolite compared to the subophitic gabbro and apatitic olivine clinopyroxenite (Fig. 12). Figs. 13–15 show that the Mg# of olivine in olivine gabbro and oxide augite

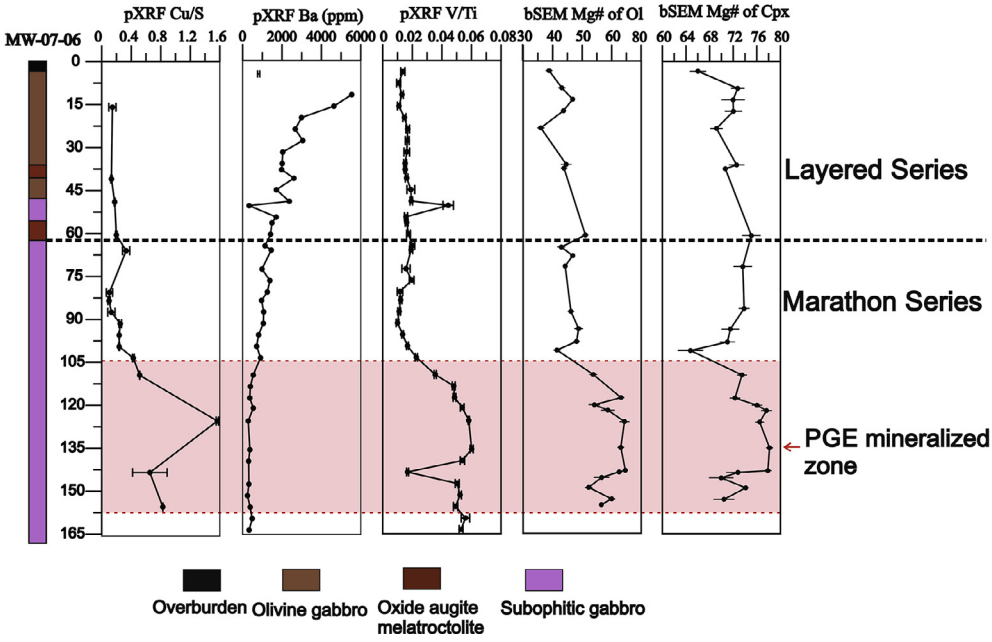

Fig. 15. pXRF and bSEM-EDS geochemical profiles down drill hole MW-07-06 at the WD zone, the shaded area indicates disseminated Cu-PGE mineralized zone. The error bar for pXRF analysis represents 2σ analytical uncertainty determined by multiple analyses on the same powder. The error bar for bSEM-EDS analysis represents 1σ sample variability determined by 3–5 analyses on 3–5 grains of each mineral type in each sample.

melatroctolite units either gently increases or decreases downhole, whereas the Mg# of olivine in subophitic gabbro and apatitic olivine clinopyroxenite is much more variable. The combination of pXRF and bSEM-EDS provide a more robust method for distinguishing units from the Layered Series units (olivine gabbro and oxide augite melatroctolite) from those of the Marathon Series (subophitic gabbro and apatitic olivine clinopyroxenite) than by pXRF analyses alone.

To evaluate whether these techniques are viable at other locations with significant Ni-Cu-PGE mineralization in the Midcontinent Rift, available published data sets were examined to determine whether the ranges of elements at these deposits are sufficient to discriminate between units. The areas examined include the Eagle Intrusion, the Tamarack Intrusive Complex, the Thunder Lake Intrusion, the Partridge River Intrusion of the Duluth Complex, and the Sonju Lake Intrusion of the Beaver Bay Complex (Fig. 1). The Eagle Intrusion is located in the Baraga Basin approximately 11 km from the Boulderdash and Roland Lake Intrusions. The latter two intrusions contain minor or negligible sulfide mineralization (Dunlop, 2013) and can be successfully distinguished from the Eagle Intrusion using the diagram of whole-rock Ba vs. V/Ti (Fig. 16A). This diagram can also be used to distinguish: 1) the mafic to ultramafic unit (main host to mineralization) from the gabbroic unit and mafic metavolcanics rocks in the Thunder Intrusion (Fig. 16B), 2) the coarse-grained olivine-bearing intrusion (main host to mineralization) from the fine-grained olivine-bearing intrusion in the Tamarack Intrusive Complex (Fig. 16C), and 3) the heterogeneous zone from the upper zone in the Partridge River Intrusion. The Mamainse Point basalts (Fig. 1) in the Midcontinent Rift are important stratigraphic markers for magmatic events in this rift. The Lower Group A of Mamainse Point basalts has been interpreted to represent the initiation of Midcontinent Rift magmatism, and which is related to Cu-Ni-PGE mineralization of the Eagle deposit and the Tamarack occurrence, whereas the Lower Group B of Mamainse Point represents a period of reduced volume of magmatism (Miller and Nicholson, 2013; Lightfoot et al., 1999; Keays and Lightfoot, 2015). The Lower Group A and B volcanics can be readily distinguished using whole-rock Ba vs. V/Ti diagram (Fig. 16C). In addition to Midcontinent Rift-related settings, the whole-rock Ba vs. V/Ti diagram can also help distinguish between the Lower Banded Series (host to the J-M reef) from the Middle Banded Series in the Stillwater Complex (Fig. 16D).

The concentrations of Ba, V, and Ti in the intrusions and volcanic rocks are above the pXRF detection limits of the Niton XL3t + pXRF analyzer (6 ppm, 15 ppm, and 30 ppm, respectively; provided by the manufacturer). In addition, the quality of pXRF for Ba and V/Ti are comparable to their lab-based counterparts (Fig. 8). Therefore, this discrimination diagram can be tested directly in the field settings of the Midcontinent Rift and Stillwater Complex to assist PGE exploration.

The Mg# of olivine and clinopyroxene, and the anorthite content of plagioclase, can also be combined to determine the chemistry of unknown units much more quickly and at lower cost than with traditional methods and be used to potentially identify mineralized rocks in other igneous settings. For example, the Sonju Lake Intrusion (Fig. 1) hosts a PGE reef, and the Mg# values for olivine and clinopyroxene increase with depth above the reef but are almost constant below the reef (see Fig. 2 in Miller, 2002). Similarly, the Lower and Middle Banded Series at the Stillwater Complex can readily be distinguished by mineral chemistry. The Mg# values of clinopyroxene and the anorthite content

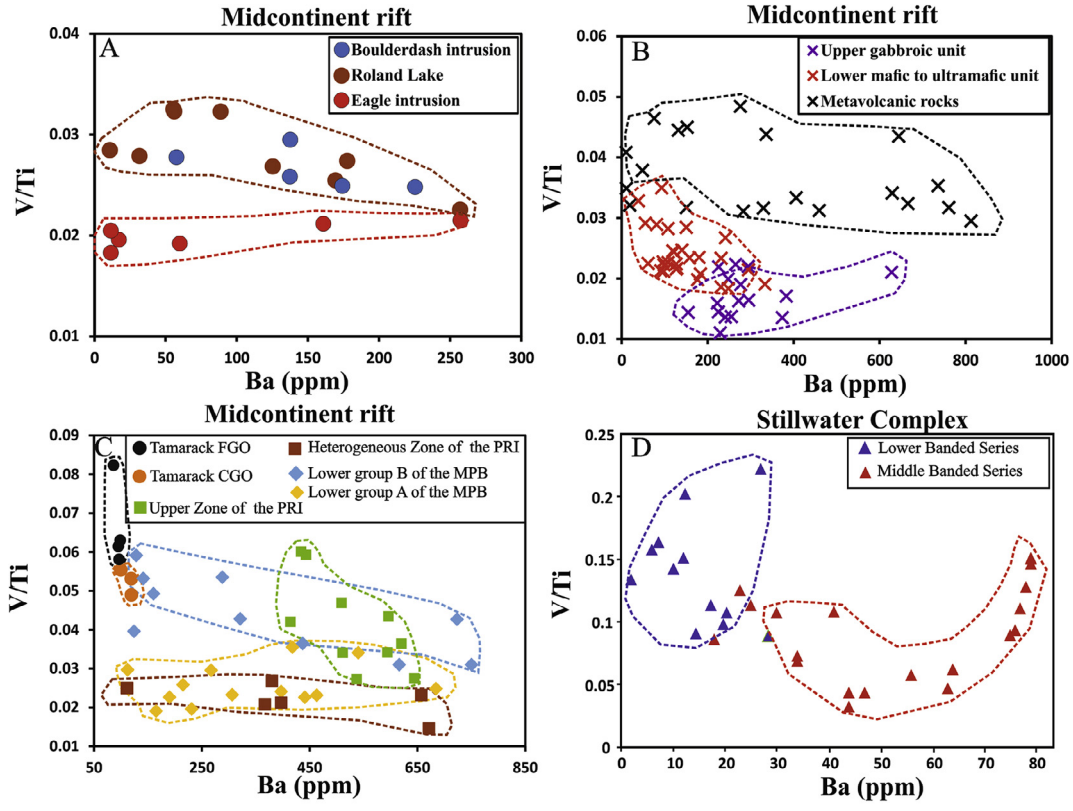

Fig. 16. Whole-rock Ba vs. V/Ti diagram highlights different zones/groups of igneous rocks in various settings within (A-C) the Midcontinent Rift and (D) the Stillwater Complex. Data for intrusions in the Barage Basin area (the Eagle, the Roland Lake, and the Boulderdash Intrusions), the Thunder Intrusion, the Tamarack Intrusive Complex, the Partridge Intrusion, and the Mamainse point basalts are from Dunlop (2013), Trevisan (2014), Taranovic et al. (2015), Taib (2001), and Lightfoot et al. (1999), respectively. Data of the Lower Banded Series of the Stillwater Complex are from Aird et al. (2017) and of the Middle Banded Series are from Meurer (1995). Abbreviations: FGO = fine-grained olivine-bearing intrusion, CGO = coarse-grained olivine-bearing intrusion, PRI = Partridge River Intrusion, MPB = Mamainse point basalts.

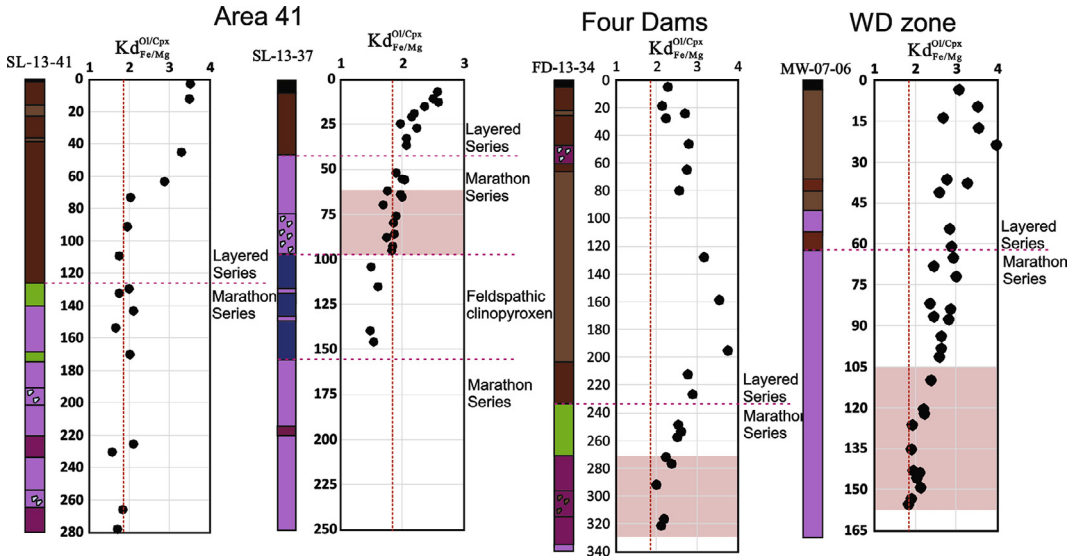

Fig. 17. Down-hole variations in Fe-Mg exchange coefficient between olivine and clinopyroxene ($Kd^{Ol/Cpx}_{Fe/Mg}$ = $(Fe/Mg)_{Ol}/(Fe/Mg)_{Cpx}$, in mole) for representative drill holes at Area 41, Four Dams, and the WD zone. Red vertical dashed lines indicate the olivine-clinopyroxene equilibrium Mg-Fe exchange coefficient (1.8) at 1400 K based on the geotheremter results of Loucks (1996). Pink boxes indicate the PGE mineralized zones. Legend for units as in Fig. 4. (For interpretation of the references to colour in this figure legend, the reader is referred to the web version of this article.)

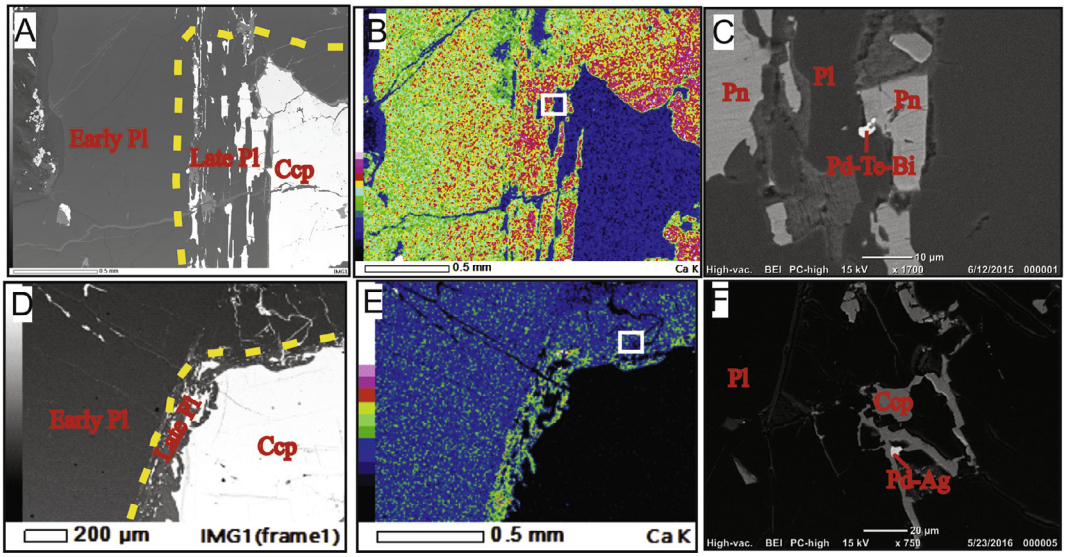

Fig. 18. Possible magma recharge evidence as reflected by the replacement of earlier less calcic plagioclase by later more calcic plagioclase, the later plagioclase occurs intergrown with chalcopyrite. PGM grains are observed in the intergrown chalcopyrite. (A)-(C) are for subophitic gabbro within the mineralized zone of SL-13-37. (D)-(F) are for subophitic gabbro within the mineralized zone of MW-07-06. The yellow dashed line highlights the contact between early and late plagioclase. The white open boxes indicate locations where PGM grains were observed. (For interpretation of the references to colour in this figure legend, the reader is referred to the web version of this article.)

of plagioclase increase with depth in the Lower Banded Series, whereas the two parameters are almost constant for the Middle Banded Series (see Fig. 6 in McCallum, 2002). The bSEM-EDS can be used to collect Mg# data of olivine and clinopyroxene, and the anorthite content of plagioclase, with data quality comparable to those acquired by electron microprobe (Cao et al., 2016; Fig. 9). Therefore, the bSEM-EDS also has the potential to rapidly distinguish rock units in a field setting to assist PGE exploration in various settings of the Midcontinent Rift and the Stillwater Complex.

7.2. Measuring apparent $Kd^{Ol/Cpx}_{Fe/Mg}$ values

Down-hole trends in the value of $Kd^{Ol/Cpx}_{Fe/Mg}$ measured by bSEM-EDS are shown in Fig. 17. The Layered Series at Area 41 and WD zone are characterized by a down-hole decrease in this value, whereas the Layered Series at Four Dams shows a down-hole increase in this value. By contrast, the Marathon Series in all three areas is characterized by small variations in $Kd^{Ol/Cpx}_{Fe/Mg}$ values; this is particularly true for the Marathon Series units within the PGE mineralized zones, where the $Kd^{Ol/Cpx}_{Fe/Mg}$ value is almost constant at around 1.8, similar to the values determined by Good (1992) for the Two Duck Lake gabbro at the Marathon deposit. This feature also differentiates these two series of rocks in the Eastern Gabbro. Furthermore, it seems that the $Kd^{Ol/Cpx}_{Fe/Mg}$ values close to 1.8 may serve as a vector to PGE mineralization in the Coldwell Complex.

The variable $Kd^{Ol/Cpx}_{Fe/Mg}$ values for the Layered Series indicate that olivine-clinopyroxene pairs in the Layered Series rocks are not in chemical equilibrium, which was interpreted by Cao (2017) to be a result

of magma undercooling. By contrast, the more constant $Kd^{Ol/Cpx}_{Fe/Mg}$ values for the Marathon Series subophitic gabbro and apatitic olivine clinopyroxenite mean that the two mineral pairs in these rocks are closer to being in chemical equilibrium. If this is correct, it seems that undercooling is not an important factor for PGE mineralization in the Marathon Series, but might be elsewhere as noted by Li et al. (2001), who proposed that undercooling is favorable for inducing the separation of an immiscible sulfide melt through lowering the sulfur solubility in the silicate magma. Therefore, acquiring $Kd^{Ol/Cpx}_{Fe/Mg}$ coefficients using bSEM-EDS to investigate possible undercooling perhaps can shed some light on Cu-PGE exploration at the Coldwell Complex and elsewhere.

7.3. Cu/S proxy for metal tenor and sulfide minerals

For mineralized rocks, high values of Cu/S correspond directly to higher proportions of chalcopyrite relative to pyrrhotite. Fig. 14 shows that the Four Dams North PGE mineralized zone has elevated Cu/S ratios compared to the Four Dams South mineralized zone, indicating that the former has higher chalcopyrite:pyrrhotite ratios, consistent with field observations. Similarly, within the PGE mineralized zones of Area 41 and the WD zone, Cu/S ratios are also significantly elevated (Figs. 13 and 15). Therefore, PGE mineralized rocks in these two areas also have greater abundances of chalcopyrite relative to pyrrhotite compared to barren rocks. These observations also suggest that high Cu/S ratio can be a good proxy for PGE mineralization throughout the Eastern Gabbro.

The high Cu/S proxy for PGE mineralization may also be applicable to other PGE deposits. PGE, particularly Pd and Pt, preferentially partition into the Cu-rich residual liquid after monosulfide solid solution (MSS) crystallization (Holwell and McDonald, 2010). Provided that the magmatic sulfide liquids fractionated MSS, Pd and Pt would be concentrated in areas where Cu-rich sulfide minerals, such as chalcopyrite, cubanite, and bornite, are abundant, all of which have high Cu/S ratios. Barnes and Ripley (2016) also suggested that the Cu-rich ores are normally enriched in Pd and Pt. Notable examples include: 1) sulfide mineralization in the Partridge River Intrusion of the Duluth Complex, where PGE-rich disseminated sulfide minerals comprise mainly chalcopyrite and pentlandite, whereas units that contain a high proportion of pyrrhotite are PGE-poor (Theriault et al., 2000), and 2) the Platinova Reef in the Skaergaard Intrusion, where magmatic sulfide minerals are present as a Cu-rich, Fe-poor assemblage (Nielsen, 2001; Holwell et al., 2015).

Both Cu and S can be acquired by pXRF, although the detection limit for S is normally high for most pXRF instruments; Hall et al. (2014) determined a detection limit of around 300 ppm S using five types of pXRF instrument. Where Cu and S are above the pXRF detection limit, their ratios are comparable to lab-based methods (Fig. 8). Therefore, although pXRF is unable to detect the low concentrations of PGE that are present in most geological materials, it still can be used to vector towards potential PGE mineralization in the Eastern Gabbro and other igneous settings by determining Cu/S ratios in the field.

7.4. Identification of possible magma recharge zones

Magma recharge is favorable for PGE mineralization because: 1) it implies the existence of a magma conduit setting, whereby PGE mineralization can be controlled by various fluid dynamic processes (cf. Naldrett and Lightfoot, 1999), and 2) the PGE tenor can be upgraded through a magma recharge process (Kerr and Leitch, 2005), thus increasing the potential for high-grade deposits. Figs. 13–15 show that the Mg# values of olivine and clinopyroxene for the Marathon Series subophitic gabbro and apatitic olivine clinopyroxenite in the three localities fluctuate over short distances, a feature that is particularly evident for the rock units within the PGE mineralized zones. This is consistent with magma recharge having occurred. A good example is SL-13-37, where the Mg# of olivine and clinopyroxene are more variable in mineralized subophitic gabbro compared to barren subophitic gabbro (Fig. 13). All subophitic rocks contain similar amounts (~10 modal %) of interstitial minerals (biotite, hornblende, etc.), which rules out the possibility that the variability of the Mg# values of olivine and clinopyroxene in the mineralized zone is the result of different amounts of trapped liquid. Instead, this observation implies a dynamic environment for formation of the mineralized zone, consistent with magma recharge. By contrast, the subophitic gabbro units in MW-07-06 from the WD zone that contain PGE mineralization exhibit a relatively small variability in the Mg# of olivine and clinopyroxene between samples, suggesting a less dynamic environment (Fig. 15). Considering that the PGE mineralization in MW-07-06 has a lower grade than that in SL-13-37, the variation in the Mg# values has the potential to be a proxy for differences in PGE grade, i.e., greater variation corresponds to a higher PGE grade. However, apatitic olivine clinopyroxenite in FD-13-34 from Four Dams, which contains a higher grade of PGE mineralization than the WD zone, also contains olivine and clinopyroxene that exhibit a small variation in their Mg# values (Fig. 14). Therefore, the greater variability of Mg# as a potential vector to higher PGE grades perhaps is only applicable to the subophitic gabbro that contains PGE mineralization. Note that Good et al. (2015) proposed that the PGE mineralization in the subophitic gabbro formed in a magma conduit, whereas mineralization in the apatitic olivine clinopyroxenite can be explained by a relatively closed system R-factor (the mass of sulfide melt over the mass of silicate magma, Campbell and Naldrett, 1979) model. Nevertheless, an initial assessment of PGE mineralization can be gained through investigating the variability in mineral chemistry, particularly for subophitic gabbro, by using bSEM-EDS prior to traditional assays, which can take weeks or more to complete.

Magma recharge zones may also be documented by the replacement of early, less-calcic plagioclase by later more-calcic plagioclase, as observed in mineralized zones in SL-13-37 and MW-07-06 (Fig. 18). Similar textures were also observed by Good and Crocket (1994) and Shahabi Far (2016) in the Marathon deposit. Shahabi Far (2016) conducted detailed LA-ICPMS studies on this plagioclase overgrowth texture and concluded that the rimmed plagioclase has distinct Fe, Sr, Ba contents, elevated Eu/Eu^{*}, and greater La, S, and base metal contents compared to the replaced plagioclase. These observations are consistent with the infiltration of a very different magma into the chamber, i.e., magma recharge, and cannot be explained by the fluid-induced Ca-Na exchange or Na loss as suggested by Benkó et al. (2015) for rocks in the Duluth Complex. It is notable that the later plagioclase occurs intergrown with sulfide minerals that show close associations with platinum-group mineral (PGM) grains (Fig. 18). This was interpreted by Shahabi Far (2016) as a sulfide liquid being present when early formed plagioclase was replaced through interaction with a late-stage hydrous melt. Therefore, using the bSEM-EDS to identify magma recharge zones is another exploration tool that seems applicable throughout the Eastern Gabbro.

Magma conduit models have been proposed for several of the ultramafic intrusions that host Cu-Ni-PGE deposits in the Midcontinent Rift, including the Current Lake deposit (Goodgame et al., 2010), the Eagle deposit (Schulz et al., 2010; Ding et al., 2012), and the Tamarack occurrence (Goldner, 2011; Taranovic et al., 2016). Examples of magma conduit settings elsewhere include the River Valley Intrusion of the East Bull Lake intrusive suite, Canada (Holwell et al., 2014), the Jinbaoshan sill, China (Wang et al., 2010), and the Noril'sk region, Russia (Naldrett et al., 1995; Naldrett and Lightfoot, 1999). In these settings, sulfides that are highly enriched in PGE were proposed to have formed by a magma recharge upgrading process as described by Kerr and Leitch (2005). This study demonstrates that down-hole variations of the Mg# values of olivine and clinopyroxene and also favorable textures from bSEM-EDS can be used to identify magma recharge zones. This method therefore can be potentially applied to conduit settings to assist mineral exploration.

8. Conclusions

The combination of pXRF and bSEM-EDS can be used to assist PGE exploration in the Midcontinent Rift and elsewhere through the following aspects.

1) Distinguishing PGE mineralization-favorable rock types from barren rock types using whole-rock V/Ti vs. Ba and mineral chemical compositions;
2) Acquiring Cu/S ratios, because high Cu/S ratios can serve as a proxy to PGE mineralization;
3) Acquiring $Kd^{Ol/Cpx}_{Fe/Mg}$ values to assess whether chemical equilibrium between olivine and clinopyroxene was established, which could help distinguish among different intrusive rocks and investigate possible magma undercooling processes;
4) Identifying favorable, PGE-mineralized magma recharge zones through investigation of down-hole profiles of the Mg# values of olivine and clinopyroxene, and their variability, as well as the observation of favorable textures such as the replacement of earlier plagioclase by later more calcic plagioclase.

Acknowledgement

We gratefully acknowledge NSERC, Stillwater Canada Inc. and the China Scholarship for funding this project. John McBride, Katrina McLean and Ryan Ruthart of Stillwater Canada are particularly thanked for their help with field work. We thank Marc Beauchamp for the assistance with electron microprobe analyses. Additional support for pXRF analyses was provided by Elemental Controls Ltd. and for bSEM analyses by JEOL. Constructive comments from Dr. Xue-Ming Yang and an anonymous reviewer are appreciated.

A. Appendix

Tables A1 and A2.

Table A1
Whole-rock Ti, Cu, S, V, Ba, Zr and ratios of V/Ti and Cu/S from pXRF for all sampled drill holes in this study. 95% confidence error for element is given in the bracket, error for the ratio represents 95% confidence error calculated based on the equation $\sigma_{(A/B)} = A/B \times ((\sigma_A/A)^2 + (\sigma_B/B)^2)^{1/2}$. Abbreviations: AC = apatitic olivine clinopyroxenite, FC = feldspathic clinopyroxenite, GA = gabbroic anorthosite, LS = Layered Series, M = Metabasalt, MS = Marathon Series, OAM = oxide augite melatroctolite, OG = olivine gabbro, OM = oxide melatroctolite, SG = subophitic gabbro.

Drill hole	Depth/m	Series	Unit	Elements					Ratios			
				Ti (2 4 0)	Cu (44)	S (2 0 0)	V (22)	Ba (22)	V/Ti	Error	Cu/S	Error
FD-13-34	5	LS	OAM	49,506	1245	4081	738	590	0.02	0.001	0.3	0.02
	9.5		OAM	27,559	454		422	798	0.02	0.001		
	14		OAM	28,764	1547	4653	723	681	0.03	0.001	0.3	0.02
	18.5		OAM	10,111	3604	15,907	274	1475	0.03	0.002	0.2	0.00
	23		OG	19,864	545		561	1206	0.03	0.001		
	27.5		OAM	44,897	2076	6852	1403	434	0.03	0.001	0.3	0.01
	32		OAM	54,727	1489	1533	1263	337	0.02	0	1.0	0.13
	36.5		OAM	21,814	1193	3560	399	898	0.02	0.001	0.3	0.02
	41		OAM	30,026	559		675	519	0.02	0.001		
	45.5		OAM	52,601	1933	6358	804	503	0.02	0	0.3	0.01
	50		AC	25,367	2570	14,271	421	1017	0.02	0.001	0.2	0.00
	60		OAM	12,408	2978	14,518	266	757	0.02	0.002	0.2	0.00
	64.5		OAM	10,290	455	775	227	914	0.02	0.002	0.6	0.16
	66		OAM	7644	194		147	1038	0.02	0.003		
	70.5		OG	16,280	179		301	720	0.02	0.001		
	75		OG	13,297	176	294	173	687	0.01	0.002	0.6	0.4
	79.5		OG	14,943	134		249	702	0.02	0.002		
	84		OG	19,981	146		214	588	0.01	0.001		
	89.5		OG	19,440	244		195	532	0.01	0.001		
	94.5		OG	21,344	97		170	629	0.01	0.001		
	99		OG	21,321	86		236	455	0.01	0.001		
	103.5		OG	30,391	107		259	468	0.01	0.001		
	108		OG	18,976	109		224	612	0.01	0.001		
	112.5		OG	32,070	622	6226	302	445	0.01	0.001	0.1	0.01
	117		OG	17,145	133		226	804	0.01	0.001		
	127		OG	20,709	174		247	602	0.01	0.001		
	131.5		OG	20,545	233	741	206	858	0.01	0.001	0.3	0.1
	136		OG	17,843	365	427	190	759	0.01	0.001	0.9	0.4
	140.5		OG	25,166	419		310	667	0.01	0.001		
	145		OG	22,903	299		297	643	0.01	0.001		
	149.5		OG	30,926	389	637	366	649	0.01	0.001	0.6	0.2
	154		OG	17,584	283		226	814	0.01	0.001		
	158.5		OG	21,752	279		264	785	0.01	0.001		
	163		OG	20,768	253		232	761	0.01	0.001		
	167.5		OG	18,444	206		274	827	0.02	0.001		
	172		OG	23,171	328		340	790	0.02	0.001		
	176.5		OG	18,221	261		230	763	0.01	0.001		
	181		OG	19,103	271		253	792	0.01	0.001		
	190		OG	17,900	289		271	866	0.02	0.001		
	194.5		OG	17,004	277		283	897	0.02	0.001		
	199		OG	20,440	327		338	803	0.02	0.001		
	203.5		OAM	23,752	279		352	639	0.02	0.001		

(*continued on next page*)

Table A1 (*continued*)

Drill hole	Depth/m	Series	Unit	Elements					Ratios			
				Ti (2 4 0)	Cu (44)	S (2 0 0)	V (22)	Ba (22)	V/Ti	Error	Cu/S	Error
	208		OAM	37,943	655		563	415	0.02	0.001		
	212.5		OAM	23,225	309		327	802	0.01	0.001		
	217		OAM	29,638	419		488	626	0.02	0.001		
	221.5		OAM	30,296	362		405	656	0.01	0.001		
	226		OAM	32,473	631		542	558	0.02	0.001		
	230.5		OAM	41,389	665		709	531	0.02	0.001		
	235		OM	57,023	759	3742	751	83			0.2	0.02
	239.5		OM	52,731	700	1597	865	139			0.4	0.06
	244		OM	43,740	626	2179	815	190	0.02	0.001	0.3	0.03
	248.5		OM	28,339	446		519	372	0.02	0.001		
	253		OM	33,368	498	1467	722	292	0.02	0.001	0.3	0.06
	257.5		OM	35,511	542	953	793	423	0.02	0.001	0.6	0.1
	262		OM	28,519	443		813	372	0.03	0.001		
	266.5		OM	23,566	847		852	399	0.04	0.001		
	271		OM	34,116	800		1730	433	0.05	0.001		
	272	MS	AC	22,738	3173	1614	1154	398	0.05	0.001	2.0	0.2
	276.5		AC	13,186	4781	6051	842	240	0.06	0.002	0.8	0.03
	281		AC	28,397	438		872	458	0.03	0.001		
	285.5		AC	12,372	364		607	363	0.05	0.002		
	291		AC	3323	3312	1411	211	245	0.06	0.008	2.4	0.3
	295.5		AC	7944	1753	1989	381	349	0.05	0.003	0.9	0.1
	302		AC	6688	1235		363	289	0.05	0.004		
	305		AC	4671	592		374	429	0.08	0.006		
	310		AC	7383	1132		455	226	0.06	0.004		
	316		AC	6905	2231	1127	495	168	0.07	0.004	2.0	0.4
	320.5		AC	5693	2710	2757	506	224	0.09	0.005	1.0	0.1
	325		AC	2100	2960	1890	177	213	0.08	0.014	1.6	0.2
	327.5		AC	1984	3904	4255	184	343	0.09	0.016	0.9	0.04
	330		AC	2699	3539	5470	232	356	0.09	0.011	0.7	0.03
SL-13-32	5.5	LS	OG	31,693	2691	7029	885	1049	0.03	0.001	0.4	0.01
	10		OG	18,948	1824	5926	448	1034	0.02	0.001	0.3	0.01
	12	MS	SG	9466	1442	5811	214	1093	0.02	0.002	0.3	0.01
	17		SG	14,676	2662	11,680	463	999	0.03	0.002	0.2	0.01
	22		SG	13,208	1355	3081	463	736	0.04	0.002	0.4	0.03
	27		SG	11,784	938	3397	403	849	0.03	0.002	0.3	0.02
	32		SG	13,489	2443	5970	433	828	0.03	0.002	0.4	0.02
	37		SG	15,813	333		560	725	0.04	0.002		
	42		SG	17,029	1064	1689	549	708	0.03	0.001	0.6	0.08
	44		OM	31,679	2798	7246	1006	559	0.03	0.001	0.4	0.01
	49		OM	21,163	1782	2587	702	446	0.03	0.001	0.7	0.06
	53		SG	20,727	876		720	508	0.04	0.001		
	58		SG	29,273	581		1104	582	0.04	0.001		
	60.5		OM	28,024	663		947	604	0.03	0.001		
	66.5		OM	19,958	643	411	741	592	0.04	0.001	1.6	0.8
	70		SG	11,820	923	2299	441	603	0.04	0.002	0.4	0.04
	75		SG	4138	261		184	636	0.05	0.006		
	80		SG	2745	119		96	562	0.04	0.009		
	85		SG	15,106	1092	1811	381	743	0.03	0.002	0.6	0.07
	90		SG	5212	685		203	960	0.04	0.005		
	150.5		AC	18,117	484		398	1250	0.02	0.001		
	155.5		AC	11,574	391	69	203	1373	0.02	0.002	6	16
	160.5		AC	14,063	573		539	446	0.04	0.002		
	165.5		AC	6766	1226	1188	466	232	0.07	0.004	1.0	0.2
	170		AC	9691	470		626	336	0.07	0.003		
	200		AC	9903	1795	6129	426	380	0.04	0.003	0.3	0.01
	204.5		AC	15,078	1358	5037	440	476	0.03	0.002	0.3	0.01
	209		AC	13,930	1359	4334	512	758	0.04	0.002	0.3	0.02
	214		AC	34,434	2035	8198	1087	288	0.03	0.001	0.3	0.01
	219.5		AC	30,276	1777	7805	476	789	0.02	0.001	0.2	0.01
	224		AC	20,445	1603	4434	434	675	0.02	0.001	0.4	0.02
	229.5		AC	8496	2396	11,294	207	749	0.02	0.003	0.2	0.01
	234		AC	17,674	1490	5523	396	646	0.02	0.001	0.3	0.01
SL-13-34	3.5	LS	OAM	48,028	73	2805	440	2461	0.01	0.001	0.1	0.02
	7		OG	13,599	63		165	3886	0.01	0.002		
	13		OG	9616	74		112	3086	0.01	0.002		
	17		OG	12,252	86		208	3479	0.02	0.002		
	20.5		OAM	31,854	92		564	2150	0.02	0.001		
	24.5		OAM	24,418	77	973	318	3594	0.01	0.001	0.1	0.05
	28.5		OAM	36,183	101	2567	529	2585	0.02	0.001	0.1	0.02
	33		OG	21,087	119	1700	361	3109	0.02	0.001	0.1	0.03
	37		OG	15,321	71		291	2514	0.02	0.002		
	41.4		OG	18,226	159	1483	334	2278	0.02	0.001	0.1	0.03
	45.7		OAM	35,986	170	2454	751	1387	0.02	0.001	0.1	0.02

(*continued on next page*)

Table A1 (*continued*)

Drill hole	Depth/m	Series	Unit	Elements					Ratios			
				Ti (2 4 0)	Cu (44)	S (2 0 0)	V (22)	Ba (22)	V/Ti	Error	Cu/S	Error
	50.1		OAM	30,645	191	1970	554	1587	0.02	0.001	0.1	0.02
	54.1		OAM	39,497	1292	22,314	738	1104	0.02	0.001	0.1	0.00
	58.9		OAM	21,574	164	1086	451	1530	0.02	0.001	0.2	0.05
	63.5	MS	SG	29,141	911	7581	659	833	0.02	0.001	0.1	0.01
	67.5		SG	10,161	1028	7739	254	1653	0.03	0.002	0.1	0.01
	71.5		SG	25,520	959	9434	472	994	0.02	0.001	0.1	0.01
	75		AC	21,941	1025	2751	732	448	0.03	0.001	0.4	0.03
	76.5		AC	19,313	1187	3636	564	746	0.03	0.001	0.3	0.02
	78.5		SG	2734	294		196	411	0.07	0.01		
	88	M	FC	2833	83		257	194	0.09	0.011		
	92		FC	3444	364		283	181	0.08	0.009		
	96		FC	4651	342		375	209	0.08	0.006		
	99.5		FC	5110	208		352	203	0.07	0.005		
	103.5		FC	6592	131		457	243	0.07	0.004		
	107.8		SG	8196	294		465	352	0.06	0.003		
	111.8		FC	6101	266		429	160	0.07	0.005		
	115.8		FC	5547	1064	994	413	166	0.07	0.005	1.1	0.2
	119.5		FC	8435	132		438	112	0.05	0.003		
	123.5		FC	5668	444		374	139	0.07	0.005		
	126.5	MS	SG	20,661	123		991	445	0.05	0.001		
	128.8		SG	1949	1685	1224	159	293	0.08	0.015	1.4	0.2
	141		SG	19,922	589	1275	821	729	0.04	0.001	0.5	0.08
	143.5		SG	12,052	1007	2071	596	426	0.05	0.002	0.5	0.05
	146.5		SG	7217	501		538	273	0.08	0.004		
	147.3		AC	14,137	1491	1707	872	298	0.06	0.002	0.9	0.1
	150.5		SG	10,677	996		705	285	0.07	0.003		
	154.5		SG	7581	464		495	281	0.07	0.004		
	159.5		SG	10,112	705	967	484	476	0.05	0.003	0.7	0.2
	163.5		SG	7821	389		314	410	0.04	0.003		
	171		SG	1725	264	901	43	809	0.03	0.013	0.3	0.08
	175		SG	2259	785	4261	40	619	0.02	0.01	0.2	0.01
	181.4		SG	5004	301		186	563	0.04	0.005		
	185.4		SG	2908	177		96	463	0.03	0.008		
SL-13-37	7.5	LS	OAM	37,818	162	2380	692	1500	0.02	0.001	0.1	0.02
	11.5		OAM	35,832	146	1800	639	1698	0.02	0.001	0.1	0.03
	15.5		OAM	37,300	162	2435	704	1325	0.02	0.001	0.1	0.02
	19.5		OAM	39,546	224	2952	793	1149	0.02	0.001	0.1	0.02
	23.5		OAM	50,571	278	2969	1054	1560	0.02	0	0.1	0.02
	28		OAM	27,495	215	1016	617	1574	0.02	0.001	0.2	0.06
	30.5		OG	25,463	200	1449	527	1772	0.02	0.001	0.1	0.04
	33.5		OAM	44,629	287	2215	891	1677	0.02	0.001	0.1	0.02
	37.5		OAM	31,234	775	7083	712	1014	0.02	0.001	0.1	0.01
	41.5		OAM	25,615	386	925	670	718	0.03	0.001	0.4	0.1
	43.1	MS	AC	9325	148		259		0.03	0.003		
	45.5		SG	15,121	302		395	1077	0.03	0.002		
	50.5		SG	14,627	176		465	831	0.03	0.002		
	52.7		SG	16,569	305	3285	350	1426	0.02	0.001	0.1	0.02
	54.5		OM	30,312	240		742	962	0.02	0.001		
	57.5		SG	20,831	1268	3141	638	621	0.03	0.001	0.4	0.03
	60.5		SG	26,931	1880	9416	841	664	0.03	0.001	0.2	0.01
	63.5		SG	27,182	538	802	939	641	0.04	0.001	0.7	0.2
	67.5		SG	7116	364	2544	193	1595	0.03	0.003	0.1	0.02
	71.9		SG	2343	49		191	274		0.013		
	79.5		SG	15,581	444	2020	515	622	0.03	0.002	0.2	0.03
	81.5		SG	10,818	555	3572	361	570	0.03	0.002	0.2	0.02
	85.5		SG	16,400	457	1762	553	768	0.03	0.001	0.3	0.04
	92.5		SG	3664	390		238	294	0.07	0.007		
	96.5	M	FC	4575	863	950	412	265	0.09	0.007	0.9	0.2
	103.5		FC	8902	505		664	172	0.08	0.003		
	107.5		FC	8915	382		703	172	0.08	0.003		
	111.5		FC	7492	1353	1356	624	151	0.08	0.004	1.0	0.2
	115.5	MS	SG	9831	649		606	310	0.06	0.003		
	117.5		AC	7701	681		610	186	0.08	0.004		
	119.5		FC	12,556	595		711	157	0.06	0.002		
	123.6		SG	17,291	1406	2541	698	137	0.04	0.001	0.6	0.05
	128.5		AC	22,216	397	1670	609	183	0.03	0.001	0.2	0.04
	132.5		AC	23,536	134		651	159	0.03	0.001		
	136.5		AC	22,631	333	8190	564	99	0.03	0.001	0.0	0.01
	140.5		AC	20,931	515	2371	606	101	0.03	0.001	0.2	0.03
	148.8		AC	11,252	489		375	125	0.03	0.002		
	152.5		AC	5917	654	3240	314	125	0.05	0.004	0.2	0.02
	157.5		SG	3836	1112	2775	213	475	0.06	0.007	0.4	0.03
	161.5		SG	8311	1102	5331	441	333	0.05	0.003	0.2	0.01

(*continued on next page*)

Table A1 (*continued*)

Drill hole	Depth/m	Series	Unit	Elements					Ratios			
				Ti (2 4 0)	Cu (44)	S (2 0 0)	V (22)	Ba (22)	V/Ti	Error	Cu/S	Error
	165.5		SG	8609	1404	8434	413	356	0.05	0.003	0.2	0.01
	169.5		SG	22,762	1412	5043	735	583	0.03	0.001	0.3	0.01
	174.5		SG	5839	1379	5609	224	363	0.04	0.004	0.3	0.01
	178.5		AC	12,538	1335	10,463	606	192	0.05	0.002	0.1	0.01
	183.5		SG	2917	1187	12,463	161	321	0.06	0.009	0.1	0.01
	187.5		SG	326	1167	8281		411			0.1	0.01
	191.5		SG	175	1177	8461		518			0.1	0.01
	195.5		SG	119	1862	12,619		523			0.2	0.01
	199.5		SG		2075	16,217		546			0.1	0.01
	203.5		SG	213	2245	15,594		564			0.1	0.01
	207.5		SG	221	1294	12,140		523			0.1	0.01
	211.5		SG	343	508	6021		567			0.1	0.01
	225.5		SG	12,988	2359	13,224	394	587	0.03	0.002	0.2	0.01
	227.5		SG	5801	533	1599	170	515	0.03	0.004	0.3	0.05
SL-13-41	3	LS	OAM	30,386	96			5439				
	7.5		OAM	41,704	82			1962				
	12		OAM	18,898	155	1978	83	4627			0.1	0.02
	20		OAM	8949	136		121	3022	0.01	0.003		
	24.5		OAM	9839	126	996	113	1896	0.01	0.002	0.1	0.05
	29		OAM	11,023	142			8519				
	33.5		OAM	21,710	112	952	115	2270	0.01	0.001	0.1	0.05
	38		OAM	20,518	131		232	4357	0.01	0.001		
	42.5		OAM	33,962	119		520	3067	0.02	0.001		
	45		OAM	19,423	104		160	3860	0.01	0.001		
	49.5		OAM	21,577	117	1386	308	3992	0.01	0.001	0.1	0.03
	54		OAM	13,668	105	916	135	3490	0.01	0.002	0.1	0.05
	58.5		OAM	12,226	139		97	3725	0.01	0.002		
	63		OAM	21,889	289	2900	327	2295	0.02	0.001	0.1	0.02
	68.5		OAM	22,823	151	1231	299	2408	0.01	0.001	0.1	0.04
	73		OAM	33,457	292	4133	611	1965	0.02	0.001	0.1	0.01
	77.5		OAM	33,770	202	2175	411	1617	0.01	0.001	0.1	0.02
	82		OAM	42,083	330	3093	578	850	0.01	0.001	0.1	0.02
	86.5		OAM	31,972	319		634	1421	0.02	0.001		
	91		OAM	39,851	409		784	1257	0.02	0.001		
	94.5		OAM	32,486	283	1094	661	1300	0.02	0.001	0.3	0.06
	104.5		OAM	21,571	370	1401	408	1337	0.02	0.001	0.3	0.05
	109		OAM	62,933	856	1526	1335	614	0.02	0.001	0.6	0.08
	116.5		OAM	24,231	379		509	1377	0.02	0.001		
	121		OAM	47,143	672	1288	993	1081	0.02	0.001	0.5	0.09
	125	MS	OM?	27,456	975	1914	690	884	0.03	0.001	0.5	0.06
	129.5		OM?	18,351	1083	3422	456	759	0.03	0.001	0.3	0.02
	132		OM	14,189	869	2458	374	958	0.03	0.002	0.4	0.03
	135		OM	23,619	1009	3284	704	686	0.03	0.001	0.3	0.02
	138		OM	21,223	1849	9985	657	525	0.03	0.001	0.2	0.01
	143		SG	10,571	2045	14,957	359	505	0.03	0.002	0.1	0.00
	148		SG	9690	1063	5459	336	580	0.04	0.002	0.2	0.01
	153		SG	13,476	245		445	559	0.03	0.002		
	167		SG	16,567	1917	5204	642	547	0.04	0.001	0.4	0.02
	169		OM	17,861	2940	9576	626	543	0.04	0.001	0.3	0.01
	173.5		OM	16,429	2081	7163	565	565	0.03	0.001	0.3	0.01
	221		AC	3422	1750	2825	434	113	0.13	0.011	0.6	0.05
	225.5		AC	2692	1265	3622	303	207	0.11	0.013	0.4	0.02
	230		AC	2854	1413	4939	331	220	0.12	0.012	0.3	0.02
	265.5		AC	2828	874	2981	312	118	0.11	0.012	0.3	0.03
	270		AC	2226	822	3715	228	468	0.1	0.02	0.2	0.02
	277		AC	3896	834	2951	398	253	0.1	0.01	0.3	0.02
MW-07-06	3.9	LS	OG	15,838	208		215		0.01	0.001		
	7.9		OG	16,426	151		177		0.01	0.001		
	11.9		OG	24,986	114		326	5540	0.01	0.001		
	15.9		OG	21,420	91	629	234	4636	0.01	0.001	0.2	0.08
	19.9		OG	20,849	119		306	2989	0.02	0.001		
	23.9		OG	18,298	123		309	2672	0.02	0.001		
	27.9		OG	17,358	108		288	3052	0.02	0.001		
	31.9		GA	11,824	103		192	2037	0.02	0.002		
	35.9		OAM	23,814	171		360	2008	0.02	0.001		
	38		OAM	27,010	113		410	1980	0.02	0.001		
	41		OAM	24,801	206	1568	401	2604	0.02	0.001	0.1	0.03
	45		GA	8556	67		163	1716	0.02	0.003		
	49		OAM	25,637	299	1706	495	2369	0.02	0.001	0.2	0.03
	54.5		OAM	20,753	165		327	1702	0.02	0.001		
	56.5		Breccia	23,610	187		382	1490	0.02	0.001		
	60.5		OAM	17,476	261	1320	305	1417	0.02	0.001	0.2	0.05
	64.5	MS	SG	13,869	124		278	1138	0.02	0.002		

(*continued on next page*)

Table A1 (*continued*)

Drill hole	Depth/m	Series	Unit	Elements					Ratios			
				Ti (2 4 0)	Cu (44)	S (2 0 0)	V (22)	Ba (22)	V/Ti	Error	Cu/S	Error
	66		OG	20,514	208	627	394	1452	0.02	0.001	0.3	0.1
	72.6		OG	8062	68		127	983	0.02	0.003		
	76.6		SG	14,103	120		276	1384	0.02	0.002		
	80.6		SG	11,923	76	725	139	1254	0.01	0.002	0.1	0.07
	83.5		SG	23,990	121	1224	291	960	0.01	0.001	0.1	0.04
	87.5		SG	23,377	84	641	260	1069	0.01	0.001	0.1	0.08
	91.5		SG	24,546	255	1017	245	1053	0.01	0.001	0.3	0.07
	95.5		SG	35,773	651	2751	481	812	0.01	0.001	0.2	0.02
	99.5		SG	33,902	437	1846	567	712	0.02	0.001	0.2	0.04
	103.5		SG	29,470	567	1324	669	908	0.02	0.001	0.4	0.07
	109.5		SG	31,985	1794	3488	1135	539	0.04	0.001	0.5	0.03
	113.5		SG	24,558	638		1179	390	0.05	0.001		
	117.5		SG	25,313	1009		1229	362	0.05	0.001		
	121		SG	20,187	1135		1085	541	0.05	0.001		
	125.5		OM	54,543	3188	2035	3173	284	0.06	0.001	1.6	0.2
	135.5		SG	25,024	625		1505	368	0.06	0.001		
	139.5		SG	17,460	436		941	303	0.05	0.002		
	143.5		SG	33,287	230	12,353	559		0.02	0.001		
	147.5		SG	18,930	1450		954	318	0.05	0.001		
	151.5		OM	27,006	1589		1412	245	0.05	0.001		
	155.5		SG	16,951	4498	5431	835	382	0.05	0.002	0.8	0.03
	159.5		SG	8947	375		500	485	0.06	0.003		
	163.5		SG	19,430	435		1030	328	0.05	0.001		

Table A2

Mineral chemical results of the Mg# of olivine and clinopyroxene, and the anorthite content of plagioclase determined by bSEM-EDS in this study. St. dev refers to 1 σ standard deviation determined on multiple analyses on 3–5 grains of each mineral type in each sample. Abbreviations: AC = apatitic olivine clinopyroxenite, FC = feldspathic clinopyroxenite, GA = gabbroic anorthosite, OAM = oxide augite melatroctolite, OG = olivine gabbro, OM = oxide melatroctolite, SG = subophitic gabbro.

Drill hole	Depth/m	Series	Unit	Mg# of Ol		Mg# of Cpx		Anorthite content of Pl	
				AVG	St. dev	AVG	St. dev	AVG	St. dev
FD-13-34	5	Layered Series	OAM	63	0.3	80	1.3	43	4.5
	18.6		OAM	62	2.6	77	1.2	47	2.5
	24		OG	53	1.4	75	1.4	46	2.2
	27.9		OAM	63	0.7	79	1.4	50	1.6
	33		OAM	64	1.4			50	2.3
	46.1		OAM	61	1.5	81	0.9	48	1.6
	64.6		OAM	58	1.3	79	0.8	46	1.6
	79.6		OG	57	1.1	77	1.6	42	2.6
	127.5		OG	46	1.4	73	1.5	41	2.0
	158.6		OG	42	1.0	72	3.3	38	2.6
	194.8		OG	43	1.9	67	1.9	33	3.4
	212.5		OAM	49	1.8	72	0.9	38	1.7
	226.3		OAM	50	1.6	74	0.9	36	2.1
	248.5	Marathon Series	OM	54	2.3	76	1.4	44	2.3
	253.1		OM	47	1.0	76	1.0	50	2.1
	257.8		OM	56	1.5	76	1.4	41	1.4
	272.1		AC	59	0.8	76	1.0	41	2.1
	276.5		AC	54	1.1	79	1.1	57	1.1
	281.1		AC	50	0.8			48	2.4
	291.5		AC	65	0.9	78	1.7	48	1.6
	295.7		AC	48	1.0	78	1.6	48	1.3
	316.7		AC	62	0.8	80	0.6	37	0.4
	321.6		AC	60	0.4	81	0.7	43	4.5
SL-13-32	6	Layered Series	OG	62	0.9	75	1.0	57	2.1
	10.7		OG	62	2.7	77	0.8	55	3.0
	17.5	Marathon Series	SG	58	1.6	69	0.8	56	2.2
	22.9		SG	64	1.4	70	1.1	54	2.3
	27.1		SG	61	2.6	73	2.6	53	1.2
	32.2		SG			72	1.2	48	2.0
	37		SG	55	2.3	71	1.3	54	2.1
	42.3		SG	59	0.9	72	1.3	52	1.9
	44		OM	65	1.2			48	1.9
	49.3		OM	59	0.7	73	1.3	53	1.1
	58.5		SG	66	0.6	78	1.5	47	1.4
	61.2		OM	65	2.2			45	2.1

(*continued on next page*)

Table A2 (*continued*)

Drill hole	Depth/m	Series	Unit	Mg# of Ol		Mg# of Cpx		Anorthite content of Pl	
				AVG	St. dev	AVG	St. dev	AVG	St. dev
	75.8		SG			73	1.8	57	2.3
	80.5		SG	63	2.0	75	1.9	54	2.0
	90.6		SG			73	2.5	48	1.3
	150.5		AC			63	1.0	41	0.6
	156.1		AC			67	0.9	49	1.5
	161		AC	59	1.2	74	1.0	49	1.3
	165.5		SG	54	0.3	62	0.8	60	2.2
	170.6		AC	61	0.4	72	1.3	55	1.3
	200.6		AC	43	0.7	64	0.7	52	0.9
	204.5		AC			67	1.1		
	209.2		AC			63	0.8		
	214.5		AC			70	1.0		
	219.5		AC			73	1.4	43	2.1
	224.6		AC			73	1.7	45	2.5
	229.6		AC			74	1.1	40	1.5
	234.4		AC			75	0.9		
SL-13-34	3	Layered Series	OAM	49	1.2	77	0.8	53	3.6
	5.1		OAM	40	1.6	72	1.2	52	1.2
	7		OG	42	1.1	70	2.5	51	0.6
	13.3		OG	42	2.8	73	1.1	54	6.5
	17.4		OG	44	1.2	72	2.0	52	1.2
	19.4		OAM	46	0.7	70	0.8	55	2.3
	23.4		OAM	48	1.5	73	1.0	51	1.9
	25.7		OAM	53	1.2	75	2.5	52	1.2
	28.1		OAM	50	1.5	74	0.8	50	1.0
	30		OAM	54	1.5	74	1.0	52	1.2
	32		OG	51	1.6	76	0.7	49	2.2
	45		OAM	55	1.2	76	1.2	52	1.2
	49		OAM	56	0.8	76	0.6	53	2.1
	53		OAM	60	1.2	77	0.8	52	1.2
	59		OAM	54	1.3	74	1.2	55	2.4
	63	Marathon Series	SG	58	0.8	76	1.5	58	1.8
	65		SG	60	0.4	77	1.1	57	3.9
	75		AC	66	1.9				
	77.2		SG	68	1.5			46	1.1
	81		SG	68	1.2	78	0.6	66	2.7
	95.5	Metabasalt	FC	74	1.4	82	1.0	66	3.0
	111.6		FC	74	0.5	81	0.8	66	3.8
	119.5		FC	75	1.3	83	1.5	57	1.9
	126	Marathon Series	SG	62	0.5	76	1.4	51	1.2
	130.2		SG	60	0.8	77	0.5	52	1.8
	140.5		SG	63	0.9	78	1.7	55	2.5
	146.9		SG			75	1.0	54	1.0
	150.9		SG			72	0.7	58	2.5
SL-13-37	7	Layered Series	OAM	54	1.2	75	0.7	50	2.2
	11		OAM	53	0.7	74	0.5	55	2.3
	13		OAM	55	0.8	76	0.6	52	1.3
	15		OAM	56	1.0	75	0.7	54	1.0
	19		OAM	59	0.7	76	0.6	51	2.2
	21		OAM	57	0.6	74	0.9	51	0.8
	25		OAM	60	0.8	75	0.7	53	1.6
	27		OAM	54	0.4	72	0.5	55	2.2
	33		OAM	59	0.4	75	0.8	51	1.5
	37		OAM	60	0.7	75	1.0	52	1.8
	48	Marathon Series	SG	64	1.1			60	3.6
	52		SG	64	2.8	77	1.1	59	1.7
	54		SG	54	1.6	76	0.7	53	2.4
	55.5		SG	57	3.7	75	2.2	39	1.3
	56		SG	59	3.2	77	0.5	59	1.4
	62		SG			68	3.5		
	64		SG	57	0.8	73	2.3	60	1.6
	65.7		SG			75	0.3	52	1.5
	70		SG	65	0.5	76	0.4	68	4.2
	76		SG	63	1.3	74	1.4	65	2.8
	80		SG	59	1.9	73	1.5	43	1.7
	86		SG			74	0.3	54	1.7
	88		SG	64	1.5	75	2.8	69	2.6
	93		SG	64	1.6	76	1.1	66	1.0
	95		SG	65	2.4	77	0.5	72	2.0
	97.2		SG			75	1.2	68	3.5
	104.5	Metabasalt	FC	67	1.2	75	1.3	70	1.7
	115.4		FC	69	0.5	78	0.8	64	1.9
	140		FC	75	0.7	82	0.6	56	2.0

(*continued on next page*)

Table A2 (*continued*)

Drill hole	Depth/m	Series	Unit	Mg# of Ol		Mg# of Cpx		Anorthite content of Pl	
				AVG	St. dev	AVG	St. dev	AVG	St. dev
	146		FC	69	0.4	78	1.0	56	1.7
	157.3	Marathon Series	SG			75	1.0	54	1.8
	167.3		SG			66	0.9	47	1.6
	170.7		SG			72	1.1	53	1.7
	172.2		SG			70	1.8		
SL-13-41	3	Layered Series	OAM	33	1.0	63	0.8	29	1.9
	12.1		OAM	45	0.7	78	3.2	45	2.4
	29		OAM			68	2.6	31	1.2
	45		OAM	54	1.3	79	1.2	44	1.7
	63.2		OAM	62	1.5	83	0.8	48	2.4
	68.7		OAM	66	1.2	78	1.5	41	1.2
	73		OAM	68	1.5	81	3.3	44	2.1
	91		OAM	62	1.3	76	1.0	47	3.4
	109.1		OAM	73	0.7	82	0.6	44	2.2
	125.8	Marathon Series	OM	55	0.6	81	1.6	57	2.7
	129.5		OM	60	0.5	75	1.0	60	2.8
	132.2		OM	72	1.2	82	0.9	53	1.3
	138.6		OM	64	1.9			50	2.6
	143.5		SG	67	4.2	80	3.6	48	1.7
	153.9		SG	65	2.2	80	3.0	53	1.8
	167.4		SG	64	3.8	81	1.5	52	2.8
	170		OM	60	1.2	75	2.3	53	1.8
	173.6		OM	60	1.1			52	2.2
	221.4		AC			75	3.0	65	3.5
	225.6		AC	72	4.2	83	1.6	53	2.4
	230.7		AC	77	0.9	84	2.9	51	2.8
	266		AC	67	0.7	79	1.1		
	270.5		AC			82	0.5	49	1.7
	278		AC	68	0.6	78	0.9	53	1.1
MW-07-06	3.4	Layered Series	OG	39	1.2	66	2.6	38	1.8
	9.4		OG	43	1.1	73	1.1	40	2.2
	13.4		OG	45	2.3	69	1.9	41	1.7
	17.4		OG	42	3.2	72	1.4	42	2.8
	23.4		OG	36	1.1	69	1.0	40	1.1
	36.2		OG	45	1.8	73	1.3	47	2.6
	37.5		OAM	42	2.6	71	0.4	39	1.3
	41		OAM	49	1.3	72	0.7	47	1.7
	54.3		SG	50	1.5	74	0.5	43	1.0
	60.8		OAM	51	0.9	75	1.5	50	2.2
	65	Marathon Series	SG	43	1.2	69	0.9		
	68		SG	47	0.6	68	1.8		
	71.7		SG	46	3.8	72	1.5		
	81.5		SG	54	0.6	74	0.5	43	2.1
	83.5		OM	41	2.0	67	0.9		
	86.3		OM	54	0.9	74	0.9	42	1.0
	87.5		OM	46	1.0	71	0.8	43	1.8
	93.5		SG	49	1.3	72	1.5	41	1.2
	98		SG	48	1.0	71	1.2	41	0.7
	101		SG	41	1.1	65	2.1		
	109.6		SG	54	1.2	73	0.8	48	1.4
	117.6		SG	63	1.0			48	1.3
	120.1		SG	54	1.8	72	0.8	37	1.4
	122		SG	59	2.2	76	0.8	51	1.7
	126		SG	64	1.6	78	0.9	52	1.4
	135		SG	63	1.0	76	0.7	52	1.6
	143		SG	65	0.7	78	0.5	52	1.2
	143.6		SG	63	0.9	78	0.6	47	1.7
	145.5		SG	57	2.5	73	1.9	51	1.3
	149		SG	52	1.1	70	2.0	56	2.1
	153		SG	60	1.0	74	0.5	52	1.8
	155		SG	57	0.5	70	1.7	54	1.3

References

Aird, H.M., Ferguson, K.M., Lehrer, M.L., Boudreau, A.E., 2017. A study of the trace mineral assemblages in the Stillwater Complex, Montana,USA. Miner Deposita. 52, 31–382.

Barnes, S.-J., Ripley, E.M., 2016. Highly Siderophile and Strongly Chalcophile Elements in Magmatic Ore Deposits. Rev. Mineral. Geochem. 81, 725–774.

Benkó, Z., Mogessie, A., Molnar, F., Krenn, K., Poulson, S.R., Hauck, S., Severson, M., Arehart, G.B., 2015. Hydrothermal alteration and Cu-Ni-PGE mobilization in the charnockitic rocks of the footwall of the South Kawishiwi intrusion, Duluth Complex. USA. Ore Geol Rev. 67, 170–188.

Campbell, I.H., Naldrett, A.J., 1979. The influence of silicate: sulfide ratios on the geochemistry of magmatic sulfides. Econ. Geol. 74, 1503–1505.

Cao, Y., 2017. Cu-Pd mineralisation and exploration geochemistry of the Eastern Gabbro, Coldwell Alkaline Complex, ON, Canada (Ph.D. thesis). Western University, London,

Ontario, pp. 471.
Cao, Y.H., Linnen, R.L., Good, D.J., Samson, I.M., Rachel, E., 2016. The application of portable XRF and benchtop SEM-EDS to Cu-Pd exploration in the Coldwell Alkaline Complex, Ontario, Canada. Geochem.: Explor. Environ., Anal. 16, 193–212.
Ding, X., Ripley, E.M., Li, C., 2012. PGE geochemistry of the Eagle Ni-Cu-(PGE) deposit, Upper Michigan: Constraints on ore genesis in a dynamic magma conduit. Miner. Deposita. 47, 89–104.
Dunlop, M., 2013. The Eagle Ni-Cu-PGE magmatic sulfide deposit and surrounding mafic dikes and intrusion in the Baraga Basin, Upper Michigan: Relationships, Petrogenesis, and Implications for magmatic sulfide exploration (PhD thesis). Indiana University, Indiana, pp. 95.
Goldner, B.D., 2011. Igneous petrology of the Ni-Cu-PGE mineralized Tamarack intrusion, Aitkin and Carlton Counties, Minnesota (M.Sc. thesis). University of Minnesota, Minnesota, pp. 156.
Good, D.J., 1992. Genesis of copper-precious metal sulfide deposits in the port Coldwell Alkalic Complex, Ontario (PhD thesis). McMaster University, Hamilton, pp. 203.
Good, D.J., Crocket, J.H., 1994. Genesis of the Marathon Cu-platinum group element deposit, Port Coldwell alkalic complex, Ontario: a Midcontinent rift-related magmatic sulfide deposit. Econ. Geol. 89, 131–149.
Good, D.J., Epstein, R., McLean, K., Linnen, R.L., Samson, I.M., 2015. Evolution of the main zone at the marathon Cu-PGE sulfide deposit, Midcontinent Rift, Canada: Spatial Relationships in a Magma Conduit Setting. Econ. Geol. 110, 953–1008.
Good, D.J., Cabri, L.J., Ames, D.E., 2017. PGM facies variations for Cu-PGE deposits in the Coldwell Alkaline Complex, Ontario, Canada. Ore Geol. Rev. 90, 748–771.
Goodgame, V.R., Johnson, J.R., MacTavish, A.D., Stone, W.E., Watkins, K.P., Wilson, G. C., 2010. The Thunder Bay North deposit: Chonolith hosted Pt-Pd-Cu-Ni mineralization related to the Midcontinent rift [abs.]: International Platinum Symposium, 11th, 21–24 June 2010, Sudbury, Ontario, Canada, Ontario Geological Survey, Miscellaneous Release-Data p 269.
Hall, G., Bonham-Carter, G.F., Buchar, A., 2014. Evaluation of portable X-ray fluorescence (pXRF) in exploration and mining; Phase 1, Control reference materials. Geochem.: Explor. Environ., Anal. 14, 99–123.
Heaman, L.M., Easton, M., Hart, T.R., Hollings, P., Macdonald, C.A., Smyk, M., 2007. Further refinement to the timing of Mesoproterozoic magmatism, Lake Nipigon region, Ontario. Can. J. Earth Sci. 44, 1055–1086.
Holwell, D., Keays, R., Firth, E., Findlay, J., 2014. Geochemistry and mineralogy of platinum group element mineralization in the River Valley Intrusion, Ontario, Canada: A model for early-stage sulfur saturation and multistage emplacement and the implication for “Contact-Type” Ni-Cu-PGE sulfide mineralization. Econ. Geol. 109, 689–712.
Holwell, D.A., Keays, R.R., McDonald, I., Williams, M.R., 2015. Extreme enrichment of Se, Te, PGE and Au in Cu sulfide microdroplets: evidence from LA-ICP-MS analysis of sulfides in the Skaergaard Intrusion, east Greenland. Contrib. Mineral. Petrol. 53, 1–26.
Holwell, D.A., McDonald, I., 2010. A review of the behaviour of platinum group elements within natural magmatic sulfide ore systems. Plat. Met. Rev. 54, 26–36.
Keays, R.R., Lightfoot, P.C., 2015. Geochemical Stratigraphy of the Keweenawan Midcontinent Rift Volcanic Rocks with Regional Implications for the Genesis of Associated Ni, Cu Co, and Platinum Group Element Sulfide Mineralization. Econ. Geol. 110, 1235–1267.
Kerr, A., Leitch, A.M., 2005. Self-destructive sulfide segregation systems and the formation of high-grade magmatic ore deposits. Econ. Geol. 100, 311–332.
Li, C., Maier, W.D., de Waal, S.A., 2001. The role of magma mixing in the genesis of PGE mineralisation in the Bushveld Complex: thermodynamic calculations and new interpretations. Econ. Geol. 96, 653–662.
Lightfoot, P.C., Sage, R.P., Doherty, W., Naldrett, A.J., Sutcliffe, R.H., 1999. Mineral Potential of Proterozoic Keweenawan Intrusions: Implications of Major and Trace Element Geochemical Data from Bimodal Mafic and Felsic Volcanic Sequences of Mamainse Point and the Black Bay Peninsula, Ontario. Ontario Geological Survey, Open File Report 5998.
Loucks, R.R., 1996. A precise olivine-augite Mg-Fe-exchange geothermometer. Contrib. Mineral. Petrol. 125, 140–150.
McBride, J., 2013. Assessment Report for Diamond Drill Drilling on the Stillwater Canada Inc. Bermuda Property, Thunder Bay Division, Ontario, pp. 39.
McCallum, I.S., 2002. The Stillwater Complex: A review of the geology. In: Boudreau, A. E., (ed.). Stillwater Complex, Geology and Guide. 9th International Platinum Symposium, Montana.
Meurer, W.P., 1995. Postcumulus processes in igneous cumulates: theory and application to the Middle Banded Series of the Stillwater Complex, Montana (PhD thesis). Duke University, Durham, pp. 417.
Miller, J.D., 2002. Stratiform PGE mineralization in the Tholeiitic Layered Intrusions of the Midcontinent rift, Northeastern Minnesota: Known Examples and Potential Targets. 9th International Platinum Symposium, Montana.
Miller, J., Nicholson, S., 2013. Geology and mineral deposits of the 1.1Ga Midcontinent rift in the Lake Superior region-an overview: Cu-Ni-PGE Deposits of the Lake Superior Region, Precambrian Research Center Professional Workshop Series PRC WS-13-01.
Naldrett, A.J., Lightfoot, P.C., 1999. Ni-Cu-PGE deposits of Noril’sk region, Siberia: Their formation in conduits for flood basalt volcanism: St John’s. Geol. Assoc. Canada 104, 195–249.
Naldrett, A.J., Federenko, V.A., Lightfoot, P.C., Kunilov, V.E., Gorbachev, N.S., Doherty, W., Johan, J., 1995. Ni-Cu-PGE deposits of the Noril’sk region Siberia: their formation in conduits for flood basalt volcanism. Trans. Instit. Min. Metal. 104, 18–36.
Nielsen, T.F.D., 2001. The palladium potential of the Skaergaard intrusion. GEUS Rep. 39, p.
Piercey, S.J., Devine, M.C., 2014. Analysis of powdered reference materials and known samples with a benchtop, field portable X-ray fluorescence (pXRF) spectrometer: evaluation of performance and potential applications for exploration lithogeochemistry. Geochem.: Explor. Environ., Anal. 14, 139–148.
Ross, P.S., Bourke, A., Fresia, B., 2014. Improving lithological discrimination in exploration drill-cores using portable X-ray fluorescence measurements: (2) applications to the Zn-Cu Matagami mining camp, Canada. Geochem.: Explor. Environ., Anal. 14, 187–196.
Ryan, J.G., Shervais, J.W., Li, Y., Reagan, M.K., Li, H.Y., Heaton, D., Godard, M., Kirchenbaur, M., Whattam, S.A., Pearce, J.A., Chapman, T., Nelson, W., Prytulak, J., Shimizu, K., Petronotis, K., 2017. Application of a handheld X-ray fluorescence spectrometer for real-time, high-density quantitative analysis of drilled igneous rocks and sediments during IODP Expedition 352. Chem. Geol. 451, 55–66.
Schulz, K.J., Chandler, V.W., Nicholson, S.W., Piatak, N., Seal, R.R., Woodruff, L.G., Zientek, M.L., 2010. Magmatic sulfide-rich nickel-copper deposits related to picrite and (or) tholeiitic basalt dike-sill complexes: A preliminary deposit model. U.S. Geological Survey Open-File Report, 2010-1179.
Shahabi Far, M., 2016. The magmatic and volatile evolution of gabbros hosting the Marathon PGE-Cu deposit: evolution of a conduit system (Ph.D. thesis). The University of Windsor, Windsor.
Shaw, C.S.J., 1994. Petrogenesis of the Eastern gabbro, Coldwell Alkaline Complex, Ontario (Ph.D. thesis). The University of Western Ontario, London, Ontario, pp. 290.
Shaw, C.S.J., 1997. The petrology of the layered gabbro intrusion, Eastern gabbro, Coldwell Alkaline Complex, Northwestern Ontario, Canada: evidence for multiple phases of intrusion in a ring dyke. Lithos 40, 243–259.
Taib, N.I., 2001. Open system magmatism, and the emplacement of the Partridge River Intrusion, Duluth Complex, Minnesota. (PhD thesis) Minnesota, pp. 187.
Taranovic, V., Ripley, E.M., Li, C., Rossell, D., 2015. Petrogenesis of the Ni-Cu-PGE sulfide-bearing Tamarack Intrusive Complex, Midcontinent Rift System, Minnesota. Lithos 212–215, 16–31.
Taranovic, V., Ripley, E.M., Li, C., Rossell, D., 2016. Chalcophile element (Ni, Cu, PGE, and Au) variations in the Tamarack magmatic sulfide deposit in the Midcontinent Rift System: implications for dynamic ore-forming processes. Miner. Deposita. 51, 937–951.
Theriault, R.D., Barnes, S.-J., Severson, M.J., 2000. Origin of Cu-Ni-PGE Sulfide Mineralization in the Partridge River Intrusion, Duluth Complex. Minnesota. Econ. Geol. 95, 929–943.
Trevisan, B.E., 2014. The petrology, mineralization, and regional context of the Thunder mafic and ultramafic intrusion, Midcontinent Rift, Thunder Bay, Ontario. M.Sc. thesis 285, pp..
Van Schmus, W.R., Bickford, M.E., Zietz, I., 1987. Early and Middle Proterzoic provinces in the central United States. In: Kroner, A. (Ed.), Proterozoic lithosphere evolution. AGU, Washington, pp. 43–68.
Walker, E.C., Sutcliff, R.H., Shaw, C.S.J., Shore, G.T., Penczak, R.S., 1993. Precambrian geology of the Coldwell Alkaline Complex. Ontario Geological Survey, Open File Report, pp. 5868.
Wang, C.Y., Zhou, M.F., Qi, L., 2010. Origin of extremely PGE-rich mafic magma system: An example from the Jinbaoshan ultramafic sill, Emeishan large igneous province, SW China. Lithos 119, 147–161.